# Dissolution-precipitation creep in polymineralic granitoid shear zones in experiments I: Strain localization mechanisms

Natalia Nevskaya[1], Alfons Berger[1], Holger Stünitz[2,3], Weijia Zhan[1], Markus Ohl[4], Oliver Plümper[4], Marco Herwegh[1]

[1]Institute of Geological Sciences, University of Bern; Bern, 3012, Switzerland
[2]Department of Geology, Tromsø University; Tromsø, 9037, Norway
[3]Institut des Sciences de la Terre d'Orléans, Université d'Orléans; Orléans, 45100, France
[4]Department of Earth Sciences, Utrecht University; Utrecht, 3584 CB, Netherlands

*Correspondence to*: Natalia Nevskaya (natalia.nevskaya@unibe.ch)

**Abstract.** Dissolution-precipitation creep (DPC) is considered as one of the main processes accommodating localized strain in polymineralic shear zones of the Earth's crust. Extensive field evidence for DPC in natural shear zones supports the importance of this process. The spatio-temporal evolution and the level of compositional heterogeneity that facilitate the nucleation of such polymineralic shear zones remain poorly understood. A series of new experiments was conducted on a granitoid fine-grained ultramylonite to different strains at 650°C, 1.2 GPa with strain rates varying from $10^{-3}s^{-1}$ to $10^{-6}s^{-1}$. In Type I experiments, a fracture was induced (prior to reaching the P,T-conditions), whereas in Type II experiments, no initial fracture was induced. Consequently, in the Type I experiments viscous deformation localized strictly within the previous fracture in a ~20 µm wide zone, with grain sizes being reduced to 150-10 nm. In the Type II experiments, viscous deformation was distributed in the sample, with grain size being reduced locally to 200-50 nm. This study supports two different hypotheses for shear zone nucleation in nature. In brittle induced strain localization, DPC will be activated and lead to a rapid and strong strain localization, producing a very weak and fast deforming high strain zone. In viscously induced strain localization (without main fracture), deformation concentrates along classical strain gradients, requiring higher shear strains to reach mechanical and microstructural steady state at slower deformation rates compared to brittle-induced strain localization. In both end-member strain localization scenarios, the dominant viscous deformation mechanism in the shear zones is grain boundary sliding combined with pinning-assisted DPC. Our experiments indicate that chemical potentials in the microstructures in combination with different strain localization types may explain the often-observed concentration of strain in fine-grained polymineralic mylonites such as in granitoids but also other polymineralic rocks (e.g. peridotites, granulites etc.) in nature.

## 1 Introduction

Strain localization in the viscous part of the lithosphere is important for regional and global scale deformation, from local shear zones to mountain building scale processes (e.g. Bercovici and Karato, 2002; Ebert et al., 2007; Goncalves et al., 2016;

Nibourel et al., 2021; White et al., 1980). Strain localization is critical for the initialization of plate boundaries (e.g. Bercovici and Ricard, 2014). The processes underlying the localization are still debated and many models exist to explain them (e.g. Bercovici and Karato, 2002; Bercovici and Skemer, 2017; Gueydan et al., 2003; Platt and Behr, 2011; Rutter and Brodie, 1988; Schmid, 1982; Tullis and Yund, 1985; Wehrens et al., 2017). One basis for their understanding is the rheology of the rocks

35 hosting the shear zones. The Earth's lithosphere consists mainly of polymineralic rocks (e.g. granitoid, peridotite, gabbro). While the rheology of monomineralic rocks is reasonably well understood, the rheology becomes increasingly difficult to understand with more mineral phases in the system.

For viscous deformation two main end-member deformation mechanisms can be distinguished: diffusion- and dislocation creep. In this study, we extend the term diffusion creep to include dissolution precipitation creep (DPC), where nucleation

40 ("neo-crystallization") and growth of new grains may occur. This appears to be the most commonly observed deformation mechanism in polymineralic shear zones (e.g. Fitz Gerald and Stünitz, 1993; Herwegh and Jenni, 2001; Hippertt, 1998; Imon et al., 2002; Kilian et al., 2011; Mansard et al., 2018; Okamoto and Hiraga, 2022; Stünitz and Fitz Gerald, 1993).

While dislocation creep is a grain size insensitive process, a fine-grained material favors deformation through grain size sensitive diffusion creep due to the increase of grain and interphase surface areas. As diffusion creep implies lower stresses or

45 faster strain rates of the deformation in comparison to dislocation creep, a switch in deformation mechanism from dislocation to diffusion creep has been considered as an important process (e.g. Rutter and Brodie, 1988; Schmid, 1982), because the effect is a weaker deformational behavior that could explain strain localization in Earth's crust. Depending on the starting grain size, different deformation mechanisms may operate (Ranalli, 1982; Rybacki and Dresen, 2004). In coarse grained (granitic or gabbro/peridotite) rocks, dislocation creep probably is the dominating deformation mechanism. The processes reducing the

50 grain size and thereby potentially causing a transition from dislocation to diffusion creep still are a matter of debate and many models exist to understand this transition. The main models include: (1) initially reduced grain size through natural inhomogeneities or brittle fracturing (Mancktelow and Pennacchioni, 2005; Pennacchioni and Mancktelow, 2007; Wehrens et al., 2016); (2) reactions and formation of new phases e.g. symplectites or phase transformations (Ceccato et al., 2018; Fitz Gerald and Stünitz, 1993; Menegon et al., 2008; Stünitz and Fitz Gerald, 1993; Stünitz and Tullis, 2001); (3) a mixture of

55 different deformation mechanisms: initially dynamic recrystallization switching to diffusion creep by subsequent phase mixing and inhibited grain growth through pinning (Bercovici and Skemer, 2017; Ebert et al., 2008; Herwegh et al., 2011; Herwegh and Jenni, 2001; Linckens et al., 2011, 2015; Olgaard and Evans, 1986; Ricard and Bercovici, 2009; Wehrens et al., 2017). The phase mixing and pinning processes are key to constrain DPC in all three models and are most efficient in polymineralic rocks – highlighting the importance of polymineralic rocks for localized shear zones in the crust.

60 We performed experiments on natural fine-grained granitoid rocks in two series of experiments. A naturally banded ultramylonite with and without an initially induced fracture was deformed at 650°C and 1.2GPa confining pressure. Although coarse grained granitic or monomineralic samples of quartz and feldspar at the same temperatures, pressures, and similar strain rates deform in a brittle to semi-brittle manner (e.g. Hirth and Tullis, 1994; Tullis and Yund, 1977), our granitoid ultramylonites deform viscously and are mechanically weak. We use samples with properties very close to what is found in nature: (1) low

65    porosity as compared to gouge samples (e.g. Pec et al., 2016), (2) induced inhomogeneity as fracture in a closed system (Tullis et al., 1990), (3) natural inhomogeneity in terms of mylonitic bands (versus e.g. aplite or granite studies by Tullis (2002), Tullis et al. (1990), Tullis and Yund (1977)) and (4) relatively low experimental temperature (compilation of experiments in Ghosh et al. (2022). This allows to study the role of different phases and phase mixing on the onset of viscous deformation in polymineralic rocks, estimate the strength of polymineralic shear zones at amphibolite facies metamorphic conditions and infer

70    different strain localization mechanisms in nature.
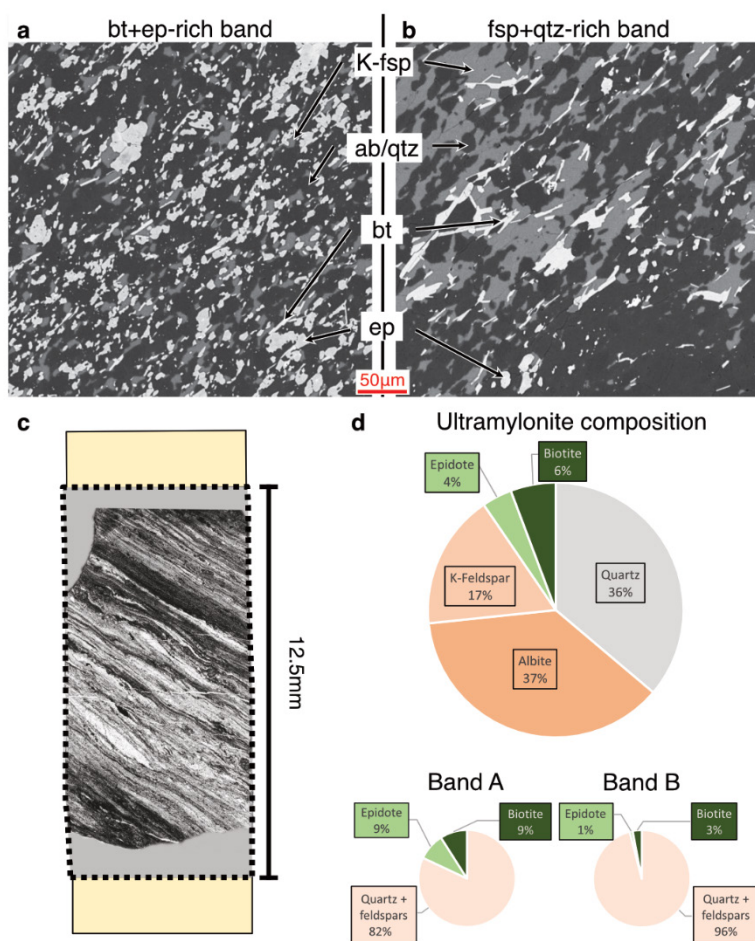
Figure 1: Starting material characterization. Ultramylonite form the Central Aar granite from Grimsel Test site underground rock laboratory. (a, b) Two endmember mylonitic bands. (a) is an ep/bt-rich band, very fine grained (<15 μm), displaying well-mixed phases. (b) is a feldspar(+qtz)-rich coarser band, where less phase mixing occurs. (c) shows foliation and mylonitic bands in experiments. Thin section PPL image of example from 634NN, loaded to experimental conditions and unloaded without imposing any additional strain to the mylonite. Zone (a) appears dark, (b) appears bright in PPL. (d) Bulk composition of the ultramylonite, measured by XRD from milled sample. py+/-wm+/-zircons appear as trace minerals. Compositions of the two band types from SEM images. More details see text and Wehrens et al. 2016 for detailed microstructural investigation of the starting material.

## 2 Materials and methods

### 2.1 Starting material characterization

The starting material is a fine-grained granitoid ultramylonite from the Central Aar granite (Fig. 1) that was cored within the Grimsel test site, an underground rock laboratory in the Central Alps. Microstructures of this ultramylonite formed during
75 Alpine peak metamorphic conditions (450°C and 600MPa, (Challandes et al., 2008; Goncalves et al., 2012)) were not overprinted afterwards, preserving the original microstructures. Additionally, the underground laboratory also allows for coring of fresh samples without any traces of weathering. Sample characterization was performed macroscopically, and through optical as well as scanning electron microscopy (SEM) (Fig. 1). The bulk mineral composition (Fig. 1d) was measured by X-ray diffraction (XRD) from a milled representative portion of the sample and further local chemistry from grey value
80 thresholding of SEM backscatter images (Fig. 1d bottom).

The bulk mylonite consists of quartz (qtz) 36 wt%, albite (ab) 37 wt%, K-feldspar (K-fsp) 17 wt%, biotite (bt) 6 wt %, epidote (ep) 4 wt%, and traces of pyrite (py) and minor accessory minerals. It is foliated, and the bands are dominated by different minerals and grain sizes. Their widths range between ~100 μm and ~400 μm. From these mylonitic bands we distinguish two end-member bands based on their grain size and composition. The most fine-grained (down to 2 μm) band is bt/ep-rich and
85 the phases are very well mixed (Fig. 1a). The other end-member band is coarser, with grains >30 μm and contains more fsp and qtz (Fig. 1b). The bt/ep-rich bands appear macroscopically dark green and microscopically dark and pleochroic (Fig. 1c). Based on these optical characteristics, most fine-grained and homogeneous areas were targeted for the experiments such that the median grain size of the samples is ~15 μm.

For the experiments, the ultramylonite was cored with a 6.33 mm drill bit such that the foliation is inclined 45° to the core
90 axis. Then each potential sample was scanned by X-ray computed micro-tomography (XRCT) in the Bruker SkyScan 1273 with 6 μm pixel size to validate that no drilling-induced fractures exist prior to the deformation. One sample (634NN) was brought to experimental conditions over-night (>8h) to check whether no grain growth or changes of microstructures of the starting material occur before deformation starts. The microstructures in this sample did not differ significantly from the starting ultramylonite (see Supplementary).
95 The grain sizes of various zones were measured by manual segmentation and calculation of the area equivalent circle diameter
$d = 2 \cdot \sqrt[2]{A/\pi}$. A statistically relevant number of grains or a representative area could not always be measured due to constraints of resolution and grain size distributions. Therefore, usually a median grain size is given, with an additional range of measured grain sizes. The median is plotted with a number-weighted density distribution and correlates well with the peak of the curve in all samples, serving as a reasonable approximation for the grain sizes in the samples
100
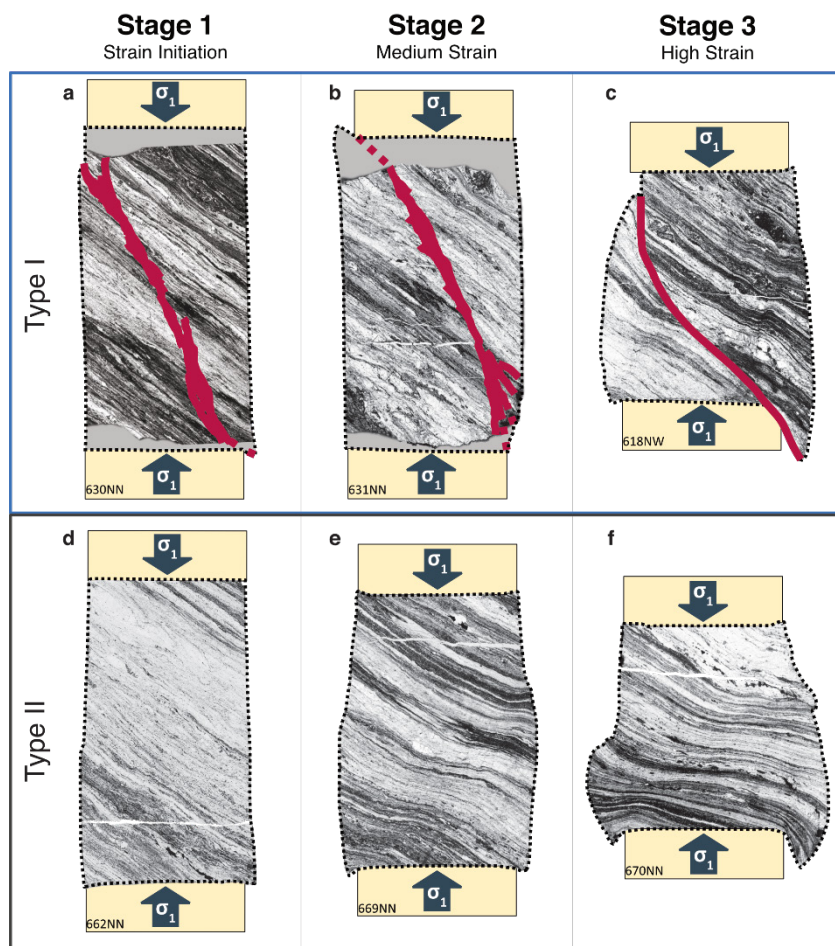
**Figure 2: Strain evolution of the two main experiment types as observed from experiments to different strains. PPL microscope images with the final sample geometry drawn manually around the samples. Shear zone orientation and localization in Type I experiments (a-c) in red, note the ~30° angle in the initial localization crosscutting the initial foliation, but dipping in the same direction. In Type II experiments (d-f), deformation is distributed, but most widening occurs at the lower 1/3 of the sample. Some corner areas are missing due to damage during polishing (grey). More details in text.**

## 2.2 Experimental setup

105   We used a Griggs type apparatus at the rock deformation lab at Orléans University, calibrated by Pec (2014). NaCl is used as confining medium for the inner and outer salt pieces. One K-type thermocouple is used to measure the temperature as input for the automated temperature control in the middle of the sample length. The samples were cut to $12 \pm 0.5$ mm length and polished plane-parallel, then dried at 125°C at least overnight and weighed dry. Welded Pt-capsules were used for all experiments. 0.025 mm thick Ni-foil was wrapped around 2-3 times, depending on the sample thickness inside the capsule.

110   Then, a controlled amount of $H_2O$ (see Table 1) was added at the bottom of the Pt-capsule before inserting the sample, thereby minimizing evaporation of water during closing and welding the capsule.

After reaching the targeted pressure and temperature conditions, the samples equilibrate for at least 1 h. Then the motor advancing the $\sigma_1$ piston is started at constant speed and moves through the top lead piece, thereby not deforming the sample significantly. The displacement, confining pressure, and load are recorded digitally in 1 s intervals and simultaneously recorded

115   with an analogue chart recorder. The hit-point, when the piston is touching the sample and actual deformation is starting, is reached after ca. 12 h. The exact position is calculated from the intersection of two slopes before and after the hit-point.

We performed experiments at 650°C, 1.2 GPa and a constant piston displacement rate of $10^{-8}$ ms$^{-1}$ (Table 1). We have two types of experiments (Fig. 2). For Type I experiments, a brittle fracture is induced during pressurization, prior to reaching the experimental P,T-conditions. For Type II experiments, pressurization of the sample to experimental P,T-conditions is

120   performed more slowly and carefully, to avoid creating loading-induced fractures. Then, a series of samples for both experiment types are deformed to different finite strains (Fig. 2), monitored by the recording of the load (Fig. 3).

The experiments are performed until peak stress, medium strain (or high strain) is reached, to reconstruct the microstructural evolution. These stages refer to the different zones in the stress-strain curve (Fig. 3c): peak stress is the point of maximum stress, after initial sample loading and possible strain initiation; medium strain is where the sample underwent some strain but is not yet in the steady state stress; high strain is the microstructure that forms at steady state stress levels.

Due to the different geometries evolving during the experiment, stresses acting on the deforming zones were corrected differently. In the Type I experiments (blue curves in Fig. 3), all the stress is assumed to concentrate on the shear zone, and the experiments are corrected as general shear experiments (mostly simple shear with a small pure shear component). These samples are deforming three orders of magnitude faster than Type II experiments. The angle and width of the shear zone are

130   considered for the calculation of shear stress and shear strain rate $\dot{\gamma}$. An equivalent strain rate $\dot{\varepsilon}_{eq}$ from the shear strain rate is calculated as $\dot{\varepsilon}_{eq} = \dot{\gamma} \frac{2 \cdot \sqrt{3}}{3}$. The acquired strain of these samples is calculated from the sample shortening as for coaxial shortening experiments, so that their finite strain is lower than that of type II samples despite their fast strain rates and high gamma values (Fig. 3). In Type II (grey curves in Fig. 3), without pre-fracture, stresses are assumed to be distributed throughout the whole cylindrical sample and are corrected as coaxial shortening experiments. A linear friction correction as in Pec, 2014

135   and Sun and Pec, 2021 was applied on all datasets. More details on the corrections are found in companion paper 2.

### 2.3 Imaging

Grain sizes ranging from >20μm down to <10nm required systematic investigation of our experiments though different scales with suitable instruments. Imaging of the samples was performed through the light microscope first, resolving grain scales of
140    mm to μm. Scanning electron microscope (SEM) analyses were performed at a Zeiss EVO50 SEM, using the backscatter (BSE) detector and energy dispersive X-ray spectroscopy (EDX) with the EDAX TEAM™ software, mostly at working distances of 8-9 mm and acceleration voltages of 10-20 kV, allowing to resolve grains on μm scale. Subsequently a high-resolution field emission gun (FEG)- Gemini SEM 450 was used at WD=5 mm, acceleration voltages of 5-8 kV, probe currents of 70-80 pA to resolve grains <1 μm.

145    After careful area selection in the FEG-SEM, (scanning) transmission electron microscopy (STEM) was finally used to resolve nm scale grains with the Thermo Fisher/FEI Helios Nanolab G3 (operator at Utrecht University, access through the EXCITE Network), requiring thin foils of selected sample areas. Two methods were used to cut the foils: classical cut with foils vertical to the thin section surface, and pyramidal cut (subsequently thinned) with the foils parallel to the thin section surface. Thereby, three-dimensional information was added to the grain orientation, shapes, and phase mixing. The highly strained and fine-
150    grained material was difficult to prepare and broke out or bent during polishing. To avoid amorphization during ion beam treatment, the polishing was stopped, even though the target thickness of 100 nm on top and <300 nm in the bottom was not reached. Note that under these circumstances, this led to an overlapping effect of minerals with grain sizes below the thickness of the samples.

### 3 Results

155    ### 3.1 Mechanical data

The data shown in Fig. 3 compares the stress-coaxial strain evolution of both experiment types and shows the force data before correcting for sample geometries. Both experiments have a very similar peak stress considering the force on the cylindrical samples. After correction for the different experimental geometries, the localized strain zones in pre-fractured Type I experiments are three orders of magnitudes faster than the coaxial shortening experiments (Type I $\dot{\varepsilon}_{eq} = 10^{-3}$ s$^{-1}$, Type II
160    $\dot{\varepsilon} = 10^{-6}$ s$^{-1}$, also see Table 1). The differential stresses at peak stress are <700 MPa in Type I, <600 MPa in Type II experiments. In Type I experiments, weakening occurs after peak stress at coaxial strains of ~7% and then an almost steady state stress of ~500 MPa is reached after >10% coaxial strain. In experiment Type II, continuous weakening is observed with increasing strain to <200 MPa at 40% shortening. The resulting strains in experiment Type I are up to γ=200, with slight variations due to varying localized shear zone widths (see Table 1). This is an advantage of this experimental setup, because such large strains
165    are commonly geometrically not feasible in Griggs type experiments but are often necessary to reach a steady-state microstructure. Despite the complex geometries and sample inhomogeneities, there is a reasonable agreement between the experimental results.

**Table 1: Summary of experimental parameters. All experiments were deformed at 650°C and 1.2GPa. The shear strain rates are calculated from final shear zone thicknesses after the experiment, as described in the Methods section.**

| Exp. No. | Type | Water ($H_2O$) | Coaxial Strain ε (%) | Shear strain γ (final) | Final shear zone thickness (mm) | Shear zone angle (°) | Piston displacement rate (m s⁻¹) | (Equivalent) strain rate (s⁻¹) |
|---|---|---|---|---|---|---|---|---|
| **633NN** | I | 0.2wt% | 7.0% | 103 | 0.010 | 35 | $1.01\cdot10^{-08}$ | $1.55\cdot10^{-03}$ |
| **631NN** | I | 0.2wt% | 5.0% | 75 | 0.010 | 35 | $1.20\cdot10^{-08}$ | $1.80\cdot10^{-03}$ |
| **618NW** | I | 0.2wt% | 27.5% | 191 | 0.020 | 42 | $1.54\cdot10^{-08}$ | $1.23\cdot10^{-03}$ |
| **630NN\*** | I | 0.0wt% | 0.0% | — | — | — | — | — |
| **634NN** | II | 0.2wt% | 0.0% | — | — | — | — | — |
| **670NN** | II | 0.2wt% | 40.0% | — | — | — | $1.61\cdot10^{-08}$ | $1.34\cdot10^{-06}$ |
| **669NN** | II | 0.2wt% | 5.0% | — | — | — | $1.55\cdot10^{-08}$ | $1.26\cdot10^{-06}$ |
| **658NN** | II | 0.2wt% | 6.8% | — | — | — | $1.36\cdot10^{-08}$ | $1.13\cdot10^{-06}$ |
| **662NN** | II | 0.2wt% | 8.0% | — | — | — | $1.33\cdot10^{-08}$ | $1.11\cdot10^{-06}$ |

170   Last column: For Type I experiments an equivalent strain rate is given, for Type II experiments a coaxial strain rate. All experiments at 650°C and Pc=1.2GPa.

**\*Exception:** Was only loaded 1.5kbar at 100°C without reaching the final experimental P,T-conditions.
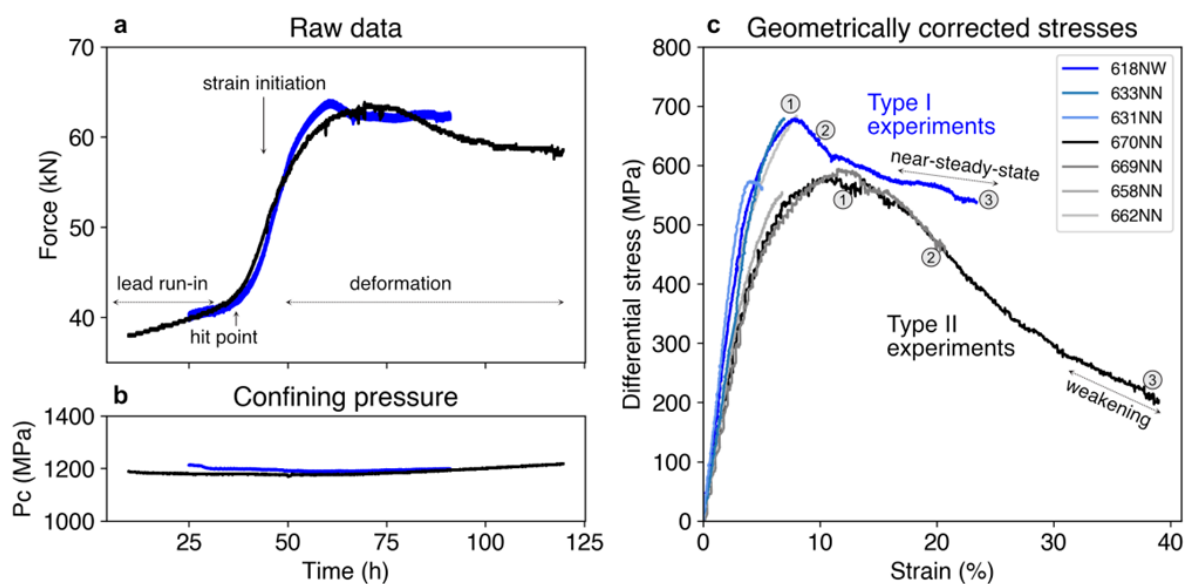
**Figure 3: Mechanical data of the presented samples. We show here the raw data of the high strain samples, that represents the force acting onto the experimental samples with the similar initial cylindrical cross-section (a) and the confining pressure (b). The corrected data for different sample geometries is displayed in (c). The onset of deformation in Griggs type experiments initiates during the slope after hit point (a). In (c), the three deformation stages as used in this study are labelled with numbers: 1 is peak stress, 2 is medium strain, 3 is high strain.**

175
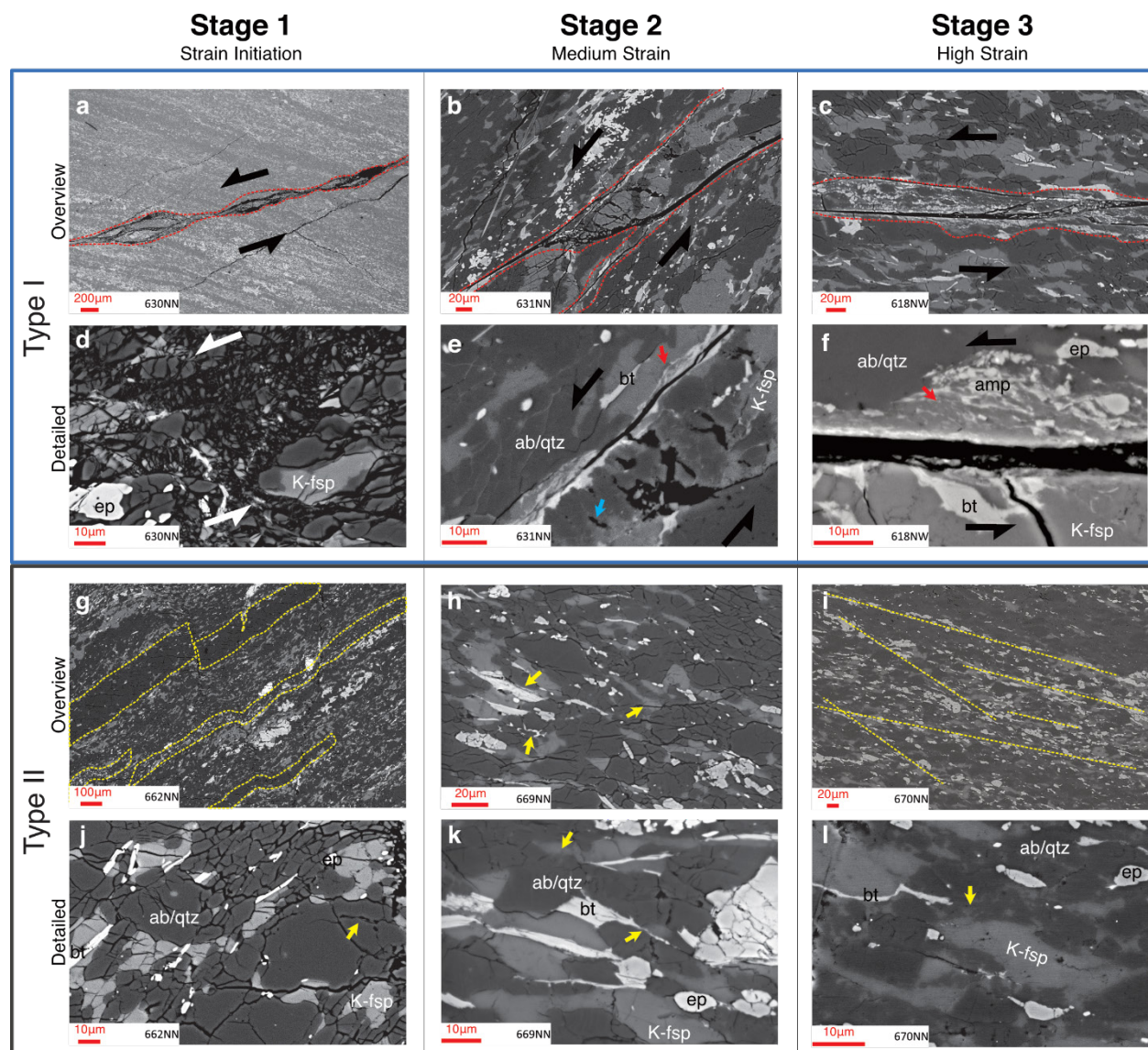
**Figure 4: Differences in strain evolution of the two main experiment types as observed from experiments to different finite strains. SEM images at low magnification to highlight the different geometries of the shear zone in Type I (a, b, c) and II (g, h, i) experiments and the details in high magnification SEM images below corresponding overview. Blue arrow in (e) points at open porosity, red arrows in (e) and (f) point at newly neo-crystallized grains. Yellow arrow in (j) shows rounded pores at a grain boundary. Yellow arrows in (h, k, l) point at newly formed grains at phase boundaries. The shear sense in Type I experiment images is indicated by arrows, for the shear zone angle please refer to Fig. 2. Compression direction is vertical in Type II experiment images. Black openings in exp. 662NN (j) occur during unloading and are relaxation cracks indicating stress concentration. Note that strain initiation in Type I experiments (a, d) occurs before the final experimental P,T-conditions are reached, while strain initiation in Type II experiments (g, j) is at peak stress in the stress-strain evolution of the sample.**

## 3.2 Microstructures – Type I experiments

In Type I experiments, the grain sizes are at first reduced in a localized fracture down to <0.5 μm, already before the experimental pressure and temperature (P,T)-conditions are reached. The fracture crosscuts the initial foliation but follows the foliation direction separated by steps. Some portions are located along the foliation and other portions are more vertical connecting to the next inclined step (Fig. 4a,d). The resulting brittle zone is undulating, and its width varies between 10 to 100 μm (Fig. 4a). This zone has a cataclastic microstructure and high porosity (Fig. 4a,d). These basic geometric and mechanical features are reproducible and are observed in all four experiments (Table 1, Fig. 3).

Subsequently, viscous deformation localizes in these fine-grained, originally cataclastic, zones. Once the P,T-conditions are reached and 5-7% shortening are applied (exp. 631NN), the viscous shear zone has a dramatically reduced porosity (Fig. 4b) and its width narrows down to ~20 μm. Grains are flattened and stretched, grain boundaries are more irregular, and a larger volume fraction of very fine grains develops (Fig. 4e). The surrounding host rock microstructures are identical to the starting material (e.g. slightly angular, same grain size; Fig. 4b). These microstructures indicate that the onset of viscous deformation was initiated within the fracture rather than in the unaffected host.

With increasing shear strain (exp. 618NW), porosity decreases further, and evolving microstructures lead to further grain size reduction in such narrow zones (Fig. 4c,f). A through-going unloading crack indicates that at a final stage, deformation localized further in a ~2 μm to 200 nm wide zone (Figs. 4c,f and 5a,d).

During all the experiments at 650°C, 1.2 GPa and fast strain rates of $10^{-3}s^{-1}$, there is no evidence for occurrence of brittle processes in the viscous strain-accommodating shear zones localized in the initial fracture (Figs. 5 and 6). On SEM scale, we find elongated biotite/ amphibole (bt/amp) grains in incompletely filled voids, indicating grain growth (Fig. 5b). Rounded pores are observed at grain boundaries and triple junctions, often within albite (ab), K-feldspar (K-fsp) and indicate dissolution or intergranular sliding processes (Fig. 5c, see Discussion). Feldspars have chemical changes and become more mixed compared to the starting material (Fig. 5c). In the following, secondary minerals that grew during the experiments are indicated with a 2 after the abbreviation, e.g. secondary K-feldspar = K-fsp2 in contrast to primary K-feldspar = K-fsp1.

In many areas, reaction microstructures of primary biotites are observed (e.g. Fig. 5d,e), leading to reduced grain sizes and nucleating new grains (as verified by TEM). Primary epidotes (and biotites) are overgrown with phases having a higher Z-contrast in BSE images. These new phases can be characterized by Fe/Mg Ca-silicate with low Al-content. These are most likely amphiboles, which cannot be identified with certainty due to their small grain sizes compared to the electron beam interaction volume (Fig. 5f), so that mixed analyses are likely. They will be referred to as amphiboles (amp) below. No amphibole was contained in the starting material, and these new minerals must have formed during the experiment.
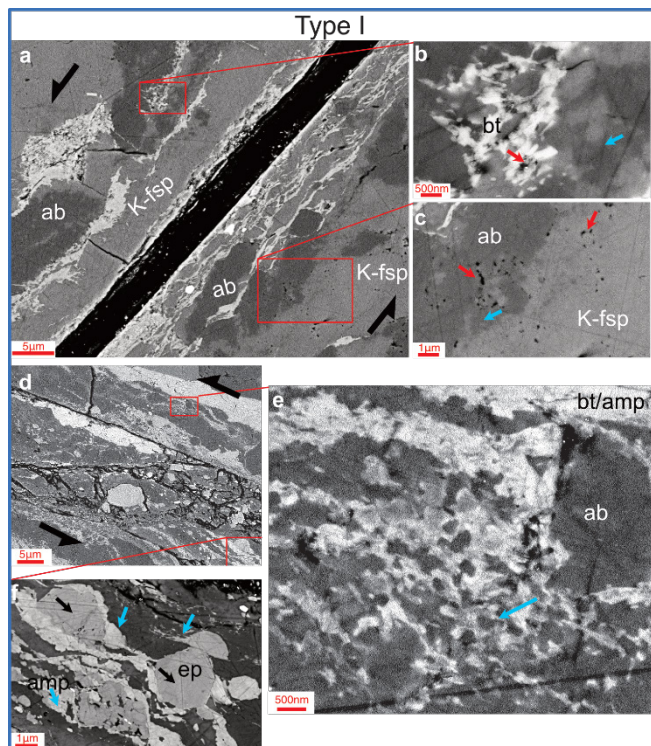
**Figure 5: Deformation microstructures in pre-cracked experiment Type I. SEM images from experiment 618nw. Overview (a) shows locations for (b), (c); overview (d) locations of (e) and (f). Note the different BSE contrasts due to different SEM beam settings in areas (a) and (d). (b): Biotite grains with open porosity (red arrow) and patchy ab/K-fsp that cannot be resolved properly in SEM BSE images (blue arrow). (c): Porosity located in between small grains and grain boundaries within/between K-fsp and ab grains (red arrow); small fsp grains (blue arrow) and brighter appearing ab/darker K-fsp between the parent grains. (e): Typical (symplectic) texture of bt and fsp, resulting in fine grains such as pointed at by blue arrow. (f): Ep1 (black arrows) overgrown by ep2/amp (blue arrows). Right blue arrow points at elongated amp forming a tail of previous ep.**

The locations of TEM foils are marked in Fig. 6a-c, with (vertical) TEM foil in Fig. 6d for overview, and a selection of TEM

210     images in Fig. 6e-l. In TEM sections, extremely fine grains (~50-200 nm) of bt, but also K-fsp, ab, qtz and ep, amp were observed. Most of such grains are dislocation- free. We see evidence for small, defect-poor grains of bt2 overgrowing bt1, while the lattice of bt1 is clearly strained with many dislocations (Fig. 6e). Other bt2 grains have idiomorphic crystal shapes, showing nucleation and growth. They often occur at grain boundaries of other phases (Fig. 6f,h). At the center of the shear zone, a thin nano-crystalline film is found (Fig. 6g). Despite the extremely fine gain size (2-15 nm), the zone is polymineralic

215     and polycrystalline, as can be seen by the lattice fringes (Fig. 6g) and chemical maps (see Supplementary).

In contrast to the relatively defect-free new grains, some old grains still have high defect densities, as for example the >500 nm size K-fsp in Fig. 6g. We assume that these grains are still primary K-fsp that were broken, most likely by the initial brittle crack (Figs. 2, 4a,d). Further, these K-fsp1-relics are also characterized by their chemical inhomogeneity. It shows a depletion in K and enrichment in Na towards its rim.

220 A few small pores, mostly associated with feldspars, were observed (Fig. 6i), indicating that the fine-grained zones might not be as dense as they appear in SEM. In many areas, the different phases are well mixed, especially in fine-grained zones (Fig. 6j,k), but locally also more monomineralic, fine grained areas exist. In those monomineralic areas, grain sizes are commonly >100 nm, whereas the very well mixed grains show sizes below 50 nm.

225
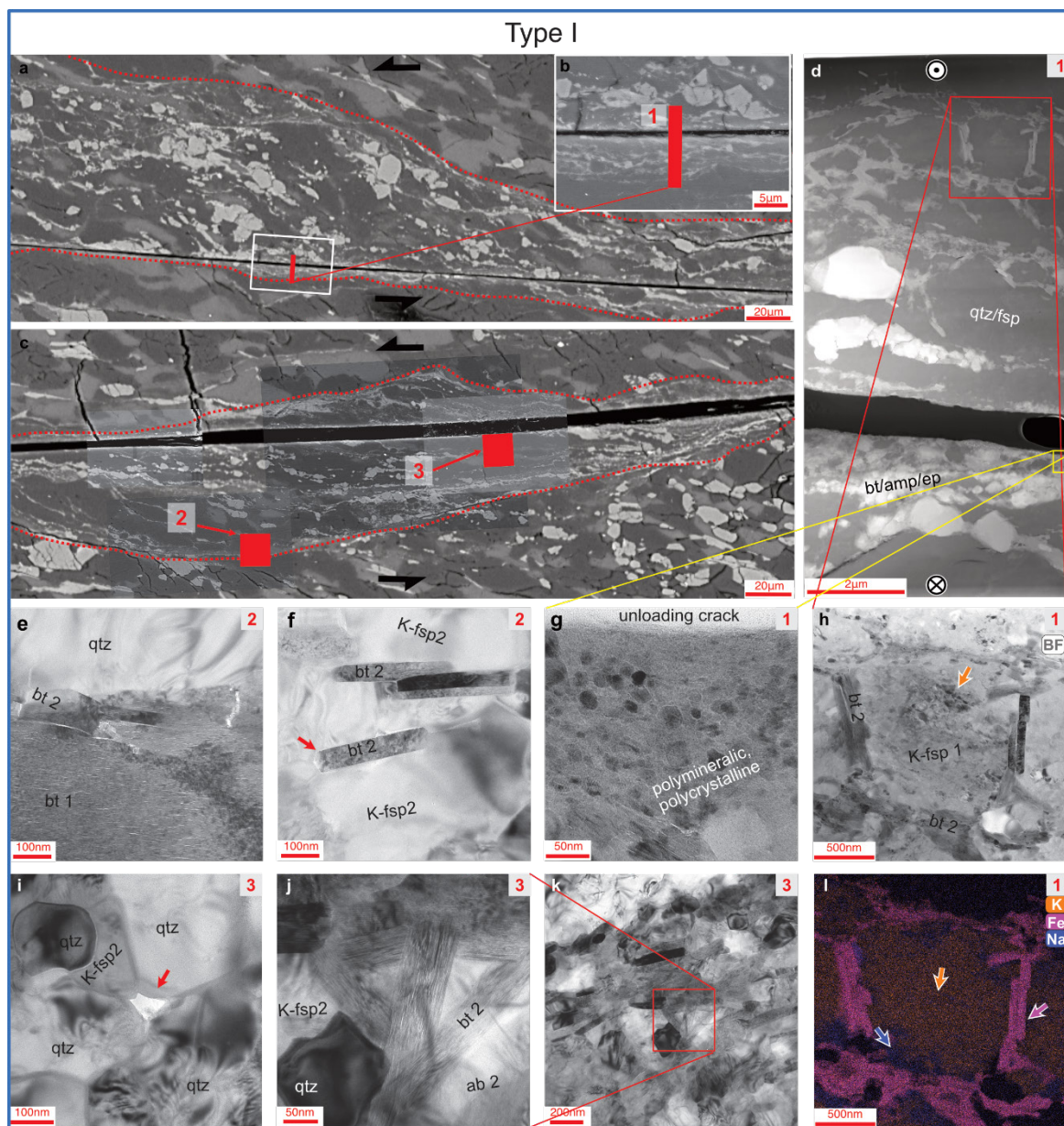
**Figure 6: TEM microstructural observations in experiment Type I. (a): SEM overview of locations for TEM sections within high strain experiment 618NW. Rectangular sections are foils cut with a pyramidal technique to allow TEM sections parallel to the thin section orientation. Elongated section 1 is a classical, vertical foil, which was oriented perpendicular to the shear zone and direction (d). Numbers indicate the TEM section appearing in top right corner in (d-l). Images (d-g, i-k) are high resolution TEM images, (h) is a STEM BF image with corresponding chemical element map in (l). Note the similar microstructures on SEM (a-c) and TEM (d) scale. (e) shows a typical overgrowth of primary bt1 by bt2. (f) shows several bt2 grains growing between K-fsp grains. Note the habit of bt2 crystals. (i) shows a pore with concave boundaries at a quadruple grain junction (arrow). The qtz grains are partially dislocation free and partially full of dislocations. (j) shows growth of bt2 grains between fsp and qtz. The qtz is completely dislocation free. (k) is an overview image for (j). (k) also shows phase mixing and a general alignment of elongated bt2/amp minerals.**

**Locations of (g) and (h) are marked in (d), a chemical map for (h) is shown in (l). (g) is a highest strain/most localized strain zone (overview in (d)). Light grey on the left is epoxy filling out the opening crack. Note the lattice fringes still visible in grains <15 nm. Just a few µm from (g) (see overview in (d)), a K-fsp grain (h, l) is overgrown by Fe-rich bt2 (right, pink arrow in (l)). The K-fsp has many dislocations (middle, orange arrow in (h)). Note also the chemical zonation of the K-fsp (orange arrow) towards the Na-richer/K-poorer rim (left, blue arrow) (l).**
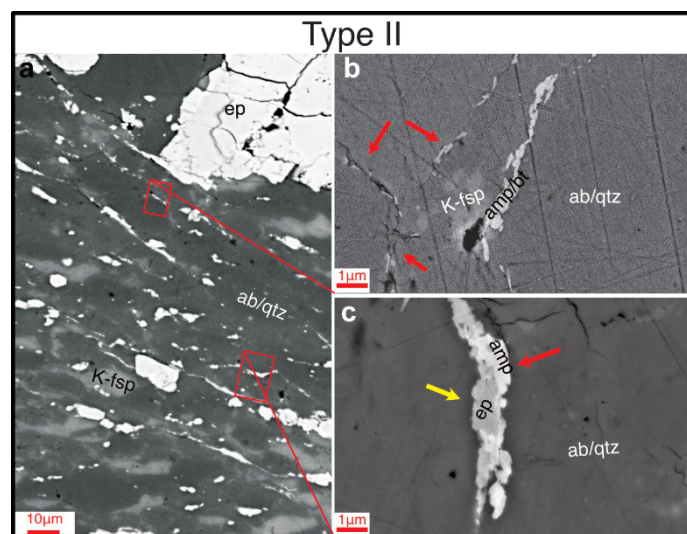
**Figure 7: SEM images of Type II experiment 670NN with various DPC-characteristic microstructures. (a): Overview image, located in the center of the sample, shortening vertically. (b) highlights nucleated bt2 at grain boundaries. (c) shows bt1 (yellow arrow) overgrown by bt2 and/or amp (red arrow).**

## 3.3 Microstructures – Type II experiments

In Type II experiments, the first stage of deformation occurs only after the final experimental P,T-conditions are reached and the sample is at differential stress (exp. 662NN versus 630NN). The first investigated stage is stopped at peak stress (exp.

230   662NN), with a slight barreling, which indicates that the strain is distributed preferentially in the lower part of the cylinder (Fig. 2d). SEM investigations show that there are conjugate shear zones developing. These are oriented ~30° to the core axis (Fig. 4g) and are connected to the corners of the bottom piston. They offset slightly the initial foliation (Fig. 4g), and the step-overs of the initial bands lead to openings, where porosity is induced. Additionally, rounded pores at grain boundaries appear (Fig. 4j).

235   With increasing strain, the barreling of the sample becomes stronger and deformation is distributed (Fig. 2e). At this stage, there is no geometric evidence for a finer grained or bt/ep-rich band to localize strain preferably with respect to a coarser or qtz/fsp-rich band. Distributed across the whole sample, minerals appear more elongated (aspect ratios of feldspar grains ~1:2.3, after initial ratios closer to 1:2). Especially grain boundaries of feldspars show chemical exchange on a small scale, which lead to new composition of the sub-micron scale (Fig. 4h,k). Bt grain boundaries are also becoming more irregular and new grains

240   (<100 nm) begin to form in their tails and at other mineral phase boundaries (Fig. 4h,k).

At high strains (bulk shortening 40%; exp. 670NN), deformation is further continuing to be distributed in the lower part of the sample. The high amount of shortening results also by material that is being "squeezed" over the bottom piston (Fig. 2f), and possibly these areas are influenced by external boundary conditions. Therefore, we focus our microstructural observations on

the central part of the sample only. There, the fsp and qtz grains are even more flattened than in the medium strained sample

245 (Fig. 4i,l, aspect ratio: ~1:2.6). The shortening leads to rotation of the initial foliation resulting in a shallower dipping angle than the initial 45°. The elongation of host grains marks two different foliations: One flat, ~75° to the core axis/principal stress and one steeper foliation at ~55° (Fig. 4i). The former, almost horizontal foliation resembles the preexisting foliation of the mylonite bands, while the latter 55° is related to the sample geometry (i.e. bottom pistons) and partially initially developed as conjugate shear zones. It is important to note that at this stage in Type II experiments, there is no evidence for any localization

250 in a narrow band.

The boundaries of two feldspars are reacting and it appears that these zones formed a fine-grained, mostly polymineralic, mixture (Fig. 4l). Fine-grained, elongated minerals (bt2 and amp) also occur at grain boundaries of other phases (Fig. 7b). The size, orientation and shape of the small bt2 indicate that these grains must have grown during the experiment. Just as in Type I experiments, primary bt1/ep1 grains are overgrown by small bt2/amp (Fig. 7c). This chemical change and growth also indicate

255 that the grains must have formed during the experiment, i.e. they are synkinematic.

On the TEM scale, we chose one area in the maximum strained sample (exp. 670NN) to investigate the tail of an elongated K-feldspar grain and the transition into albite (see above; Fig. 8a). The primary K-fsp visually has an extremely high dislocation density (Fig. 8b), whereas at its rim, new small K-fsp and ab grains occur with partially no dislocations or very low dislocation density (Fig. 8b). The K-fsp and ab are only slightly mixed but, in some areas, very fine-grained ab is found within the initial

260 and new K-fsp grains (Fig. 8b). Pores (~50-60 nm) are observed at grain triple-junctions and grain boundaries (Fig. 8c,d), and the finest observed grains have a similar grain size range (Fig. 8d). No significant changes in the chemical composition of the initial K-fsp towards the ab boundary were observed.
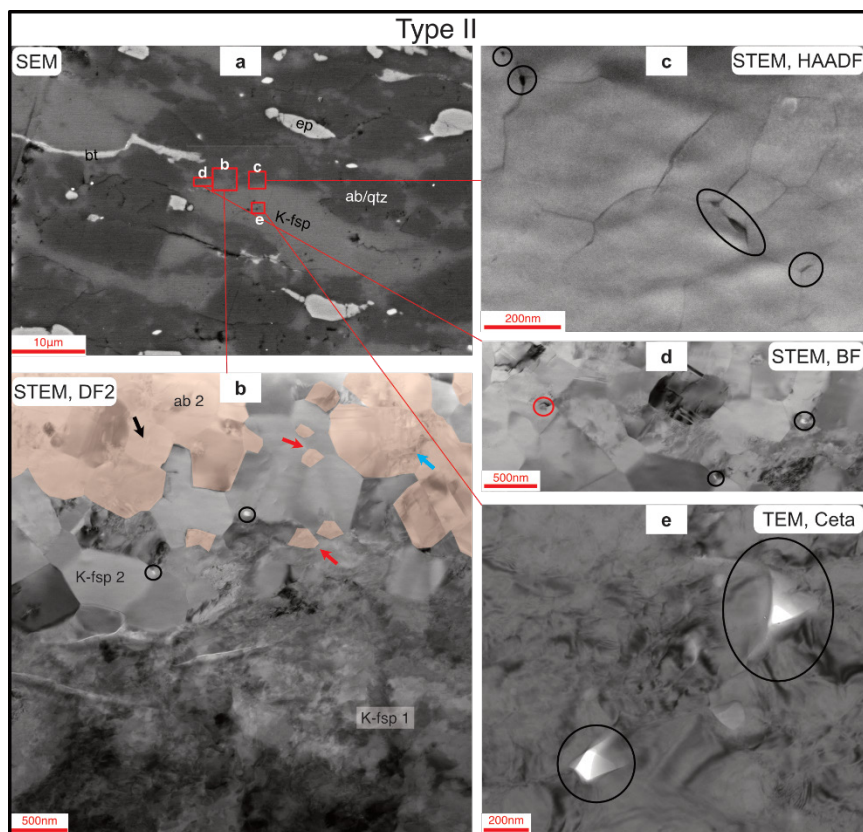
**Figure 8: TEM of phase boundary between K-feldspar and albite in high strain Type II experiment 670NN. (a): SEM image shows location of TEM foils at the rims of larger host grains. The K-fsp/ab interface does not appear sharp at this magnification, indicating that the resolution is not sufficient to resolve the grain sizes. (b): TEM foil, DF2 image with ab highlighted based on chemical maps (Supplementary). K-fsp1 shows a high dislocation density, while dislocation-free grains of K-fsp2 and ab2 (like the black arrow) occur at the phase boundary. Blue arrow points at dislocations inside of fine, newly formed ab2. Grains such as indicated by black or blue arrows are counted as large (L), isolated and small grains of one fsp inside of other fsp phase (red arrows) are counted as small (S) in the following grain size analysis Fig. 9. Black circles in (b, c, d, e) highlight open pores at triple-grain junctions and grain boundaries. In (d), red circle shows a nucleated grain with the same size as open pores in the same zone. Pores in (c, d) are in the polymineralic area containing K-fsp2 and ab2, while the pores in E are within the K-fsp1 host grain.**

265
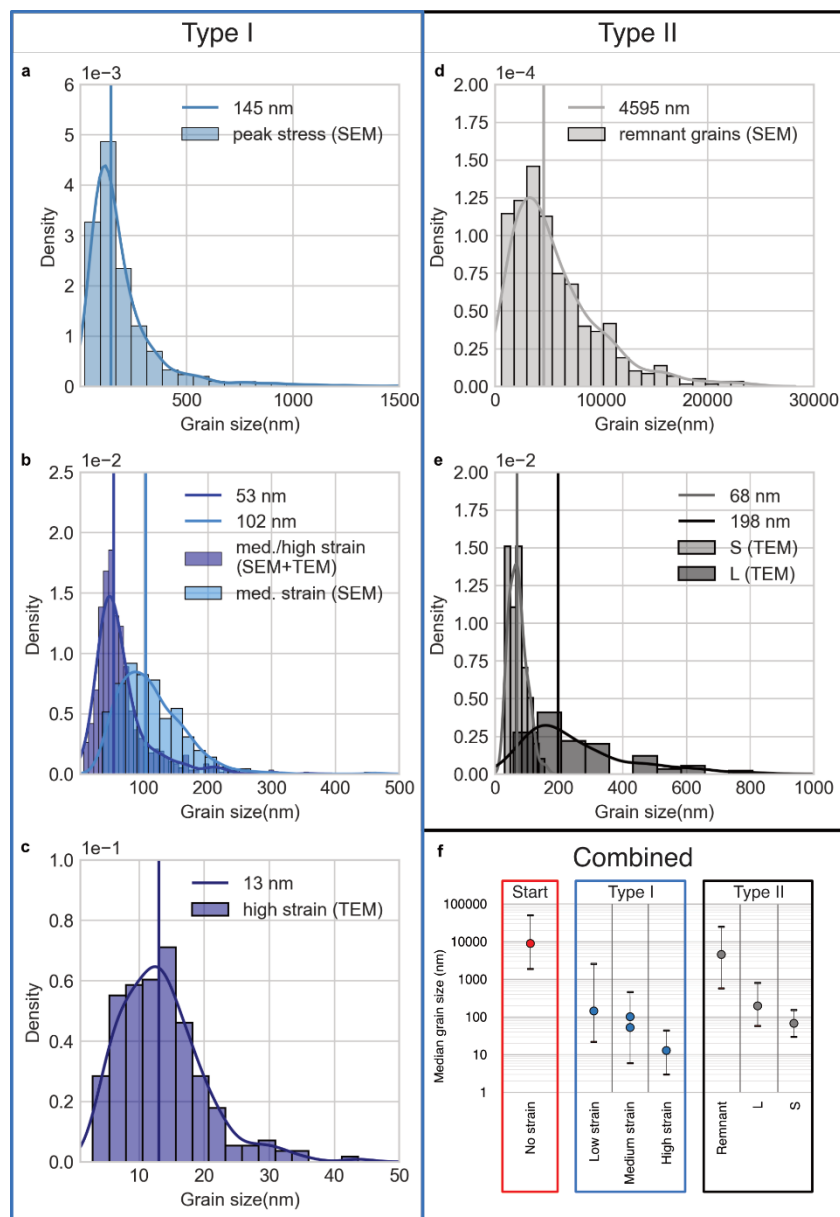
**Figure 9: Grain size distributions in pre-fractured (Type I) and not pre-fractured experiments (Type II) and a comparison with the starting material. Grain size reduction to distribution (a) occurs at peak stress, reduction to (b) after shearing to medium strain, and (c) occurs only after shearing to very high strains. All these grain sizes are still present and were measured in the high strain experiment 618NW. (d) shows the grain size distribution of elongated large grains in high strain sample 670NN, while (e) shows the measured grains in fine-grains zones between these grains. "S" refers to isolated small grains, while "L" refers to larger, often clustered grains (see Fig. 8). For a discussion on grains accommodating the strain, see text. Grain size reduction in two types of experiments on a logarithmic scale. The lines in the bar diagrams indicate median values. The dots in F represent the median grain size, while the error bars indicate the maximum and minimum grain sizes measured in the respective samples/zones. Type I grain sizes are measured in sample 618NW, Type II grain sizes in sample 670NN. All grain sizes are formed at different stages but still occur at the same time in the final experimental microstructure. See for text for definitions and further discussion if all grains still accommodate the strain in the final microstructure.**

### 3.4 Grain size evolution in both experiment types

We investigated the grain sizes in both types of experiments and grouped these into different strained zones based on the microstructural observations and spatial distributions (Fig. 9).

270 In Type I experiments, the grain sizes are measured in the different zones of sample 618NW under the assumption that they also represent the different stages of deformation (e.g. grain size gradients on SEM and TEM scale in Fig. 6). In Fig. 9a-c we differentiate between peak stress, medium strain, and high strain grain sizes. We assume that the corresponding grain sizes are formed at the respective strains.

At peak stress in Type I experiments, the sample is reduced to a median grain size of 145 nm (equivalent to microstructures in
275 Fig. 5b). There are still remnant grains from the initial brittle fracture (Fig. 5a) covering a nm to μm range (22 nm to 2.6 μm; Fig. 9a). Then, with increasing strain, grain sizes are reduced in these areas (as seen in e.g. Fig. 5E,6E,F,H-L) to medians of 102 and 53 nm (measured by SEM and TEM, respectively; Fig. 9b). This grain size is at the lower limit of SEM and upper limit of TEM resolution. Therefore, both together give a more indicative grain size range of 6 to 463 nm. The grain size in the narrow (<200 nm) zone in Fig. 5d,g reduces to a median of 13 nm with a range of 3 to 44 nm (Fig. 9c).

280 It is to be noted that with each grain size reduction step also the zone in which the strain is accommodated narrows (see companion paper 2). As a result, with a constant vertical displacement, the actual strain rate accelerates, and the grain size reduces gradually. This relationship becomes relevant for the stress-strain evolution and grain size sensitivity of the samples which is discussed in detail in companion paper 2.

In Type II experiments, two types of grain sizes are differentiated. Very fine grains, that are difficult to resolve with the SEM,
285 occur at phase boundaries of large feldspars. The large grain size is manually drawn in SEM images and a median of 4.5 μm, with a range of 580 nm to 25 μm is obtained (Fig. 9d). These largest grains are only ~50% smaller than the starting grain size of the initial ultramylonite (see also Fig. 10) opposed to the very fine grains. In the fine-grained zone between the remnant grains, two different grain sizes are differentiated: (1) small grains (named group "S") are isolated phases between the other type of feldspar; (2) larger grains (named group "L") represent monomineralic clusters of small grains (derived from one fsp).

290 We measure median grain sizes of 198 nm in the "L" feldspars, with a range of 58-808 nm (darker histogram in Fig. 9e). The "S" grain size median is 68 nm with a range of 30 to 155 nm (brighter histogram in Fig. 9e).

295

## 4 Discussion

### 4.1 Deformation mechanisms

#### 4.1.1 Evidence for dissolution-precipitation creep

In both experiment types, after deformation, all phases of the starting material (qtz, both fsp, bt/ep) are still observed, even in
300     fine-grained zones, but slight chemical changes occur as well as the formation of new amphibole. We measure chemical changes in the feldspars, too (e.g. Fig. 6h,l). Furthermore, some biotites have an Fe-enrichment with respect to the precious biotites. In addition, the two groups (old and new grains) can be discriminated by high dislocation density versus almost dislocation free grains. The chemical changes and -gradients show that the grains must have reacted during the experiment indicating existence of local chemical potentials for ionic exchange at experimental P,T-conditions.

305     With the low stresses measured for the deformation (far below the Goetze criterion $\sigma_D \geq P_c$), it is very unlikely that the extremely fine grains (observed in the high strain samples in Figs. 6g, 9c) have formed by brittle processes. The elongated minerals are parallel to the shear plane (Fig. 6d,f,k) or filling gaps between grains as in Fig. 6h. Coupled with the densely packed phases, small grain size and narrow size range , and their distinct crystal habitus, this geometry suggests stress-oriented growth (Imon et al., 2004) rather than rigid body rotation of grains after fracturing.

310     In Type II experiments three types of feldspar grains were identified, where relict grains have a high dislocation density, whereas L and S grains have distinctive low dislocation densities (as in Figs. 8 and 9). The newly formed L-grains have a broad grain size range, while the S-grain size range is narrower, but there is an overlap in their distribution. The newly formed grains have only a very slight change in chemistry compared to their host grain/porphyroclast. (Slight) phase mixing between ab2 and K-fsp 2 (Fig. 8b), dislocation-free grains, and partially well-developed grain triple junctions (Fig. 8b) indicate
315     nucleation and growth rather than dynamic recrystallization via subgrain or bulging recrystallization. The occurrence of pores along grain boundaries and grain triple junctions (while the nucleated grains "S" have a similar size compared to that of the pores) shows that the opening and filling of the pores occurs simultaneously through grain boundary sliding and rapid nucleation within the opened cavity (Ebert et al., 2007; Herwegh et al., 2011; Herwegh and Jenni, 2001; Linckens et al., 2011, 2015). The formation of these synkinematic boundary pores has first been described for geomaterials by Etheridge et al. (1984)
320     and rock analogue materials by Ree (1994). More recently, the process has been referred to as creep cavitation (Fusseis et al., 2009; Gilgannon et al., 2017, 2021).

All observations of mechanical data, chemical changes, dissolution and growth of minerals, and grain size reduction given above clearly demonstrate that the predominant deformation mechanism in both types of experiments is dissolution precipitation creep (DPC) rather than dislocation creep or frictional flow. The chemical potential mentioned above promotes
325     diffusive transport, while opening of nanometer-scale voids in dense high strain areas by grain boundary sliding (GBS) serve as nucleation sites for new precipitates. Any DPC mechanism results in a polymineralic mixture, where phases are pinning each other inhibiting/reducing grain growth (e.g. see Herwegh et al., 2011 and references therein), thereby enhancing efficiency of DPC in fine-grained pinned parts of the polymineralic mixture. The pinning leads to a stable microstructure and

differentiates the DPC process in our polymineralic rocks from DPC in monomineralic systems. Phase mixing and pinning

330    may be the reason for the onset of DPC in our samples at considerably lower temperatures than, for example, observed in monomineralic quartz (e.g. Ghosh et al., 2022, 2024; Richter et al., 2018).

The DPC in our experimentally deformed polymineralic granitoid mylonites has far reaching consequences. The occurrence of viscous deformation in our samples at 650°C versus mostly frictional deformation in coarser granites in other experimental studies conducted at the same temperature (Pec et al., 2016; Pec and Al Nasser, 2021) demonstrates that the initial grain size

335    is very important for a brittle to viscous transition (Sun and Pec, 2021). In our case, an ultramylonite with a median grain size of ~10 μm is sufficient to activate DPC at relatively fast strain rates of $10^{-6}s^{-1}$ and locally even faster. At these experimental conditions, onset of DPC cannot be predicted from monomineralic quartz flow laws (e.g. Fukuda et al., 2018; Ghosh et al., 2022; Hirth et al., 2001) and should be investigated experimentally for other polymineralic rocks in the future also.

### 4.1.2 Rate-limiting steps

340    The rate of DPC is controlled by the rate limiting step of one of the major processes (dissolution, transport, precipitation; Gratier et al., 2013; Raj, 1982; Rutter, 1976). In monomineralic systems or in metals, transport (i.e. diffusion) generally is assumed to be rate limiting. In these chemically and crystallographic simple systems, the dissolution and precipitation process is described by well-defined source and sink terms (e.g. Raj, 1982). In our polymineralic system, transport and source/sink terms are not defined, and the introduction of a chemical driving force will be necessary. Consequently, a quantitative

345    evaluation is not feasible. In the following section, we attempt to assess these parameters qualitatively.

In pressure solution or diffusion creep models, minerals dissolve at high pressure sites and precipitate at low pressure sites (Arzt et al., 1983; Elliott, 1973; Gratier et al., 2009; Niemeijer et al., 2002; Weyl, 1959; Wheeler, 1992). Often, the precipitates overgrow an existing grain leading to a change in its shape. In polymineralic systems, as in this study, an extremely fine-grained, partly equigranular, polymineralic mixture of phases indicates that the precipitates preferably nucleate and grow, as

350    this mixture could not have formed though dynamic recrystallization (Ebert et al., 2007; Herwegh et al., 2005, 2011; Linckens et al., 2011, 2015). Another component during dissolution and precipitation is the transport of the material from source to nucleation site. This transport is assumed to be diffusive along grain boundaries. The phase mixing in the fine-grained zones indicates that the diffusion length scale typically exceeds at least one grain size length in the deforming zone (largest grains being ~200 nm). K-fsp1-ab1 phase boundaries in Type II experiments do not show much phase mixing or transport of, e.g. bt2

355    or amp into the fsp. Similar observations were made in the lower strain areas in Type I. Hence, the diffusive transport length at least the grain size and is influenced by porosity/permeability. Therefore, the transport of elements through the system might be more efficient than in classical pressure solution (Wheeler, 1992) and is enhanced by initial porosity from the initial brittle fracture and phase mixing as in Type I experiments.

The growth of grains, as it is typically observed in monomineralic systems, is inhibited/reduced through pinning by other

360    phases. Brodhag et al. (2011) demonstrated that under static conditions, coupled grain coarsening occurs, where the aggregate coarsening depends on growth kinetics, as well as amount, size and spatial distribution of the slow growing phase (Herwegh

et al., 2011). Ebert et al. (2008), Herwegh et al. (2005, 2011), and Linckens et al. (2011, 2015) showed that coupled grain coarsening also occurs in naturally deformed polymineralic mylonites, with grain sizes being indicative for specific physical deformation conditions. Based on our new experimental insights we infer that the dissolution rate of minerals is enhanced by
365 a high dislocation density in parent grains, and at the same time assisted by chemical driving potentials. Fast dissolution rates may counteract grain growth if newly nucleated grains are being dissolved as well. In the case of our granitoid mylonites, the combination of the three key parameters leads to more efficient strain accommodation than in coarse or monomineralic samples, accommodating fast strain rates of $>10^{-3}s^{-1}$ (see companion paper 2).

In high strain samples of Type I experiments, there is no evidence for one of the phases being an inhibiting factor in the overall
370 dissolution and precipitation cycle, since all the phases, including quartz, are observed in the highly localized zone. Hence, instead of a single volumetrically dominating matrix phase with small amounts of a second phase (Herwegh et al., 2011), in our experiments pinning of all phases (see quantities above) by each other leads to a locally stable microstructure in a small-scale micro-chemo-mechanical equilibrium that is specific to the polymineralic assemblage. The dominant operation of DPC because of a stable small grain size results in a weak rheology and viscous behavior for all phases in the system at low
375 temperatures but fast strain rates, which would not be possible in monomineralic systems. This is supported by extrapolation to natural conditions and comparison with various quartz and feldspar flow laws in companion paper 2.

### 4.1.3 Role of feldspars for dissolution-precipitation creep

With stable and coexisting qtz, K-fsp, ab, ep/bt and amp, our polymineralic system is too complex and our current knowledge too limited to combine the role of the growth/dissolution kinetics and spatial distribution of individual minerals quantitatively.
380 However, we can focus on the feldspar system, given its volumetric dominance in our samples, which is ~54 wt% (albite 37 wt% & K-feldspar 17 wt%). Especially at the interface of K-fsp and ab grains in Type II experiments, the role of reactions between feldspars towards their stable end member composition becomes important (e.g. Fig. 8). As known for the different solvi in feldspars (e.g. Fuhrman and Lindsley, 1988), the K-fsp component in the Na-feldspar and the ab component in the K-feldspar is increasing with temperature. Fig. 10 shows the expected feldspar compositions for starting material and experiment
385 in a calculated binary phase diagram. In our samples, we see this change in compositions qualitatively, for example in Fig. 6l. Owing to this exchange, we observe in SEM images the backscatter contrast of albite becoming higher in areas of contact between K-fsp and ab, where compositions approach equilibrium compositions. Hence, in our granitic system at 650°C and 1.2GPa, chemically induced driving potentials for dissolution and precipitation of feldspars become important, especially in fsp-rich areas like band type B (Fig. 1b,d).
390 It has been inferred by various studies from the field and from experiments how the reactivity of feldspars might lead to enhanced solubility and efficient grain size reduction (Fitz Gerald and Stünitz, 1993; Hippertt, 1998; Marti et al., 2018; Stünitz and Fitz Gerald, 1993; Stünitz and Tullis, 2001). This is also supported by the very fine grains nucleating at the phase boundaries between K-fsp and ab in experiment Type II (Fig. 8). The observed microstructural evolution is very similar to feldspar-rich polymineralic experimental samples of e.g. Marti et al. (2018) or natural examples of e.g. Behrmann and

395   Mainprice (1987), Lee et al. (2022), or Menegon et al. (2008), where DPC accommodated or accompanied by mineral reactions
is inferred, pointing at an applicability of our observations beyond granitic systems. This focusses the key parameters needed
to activate the observed type of DPC to fine grain sizes, phase mixing and chemically induced driving potential.
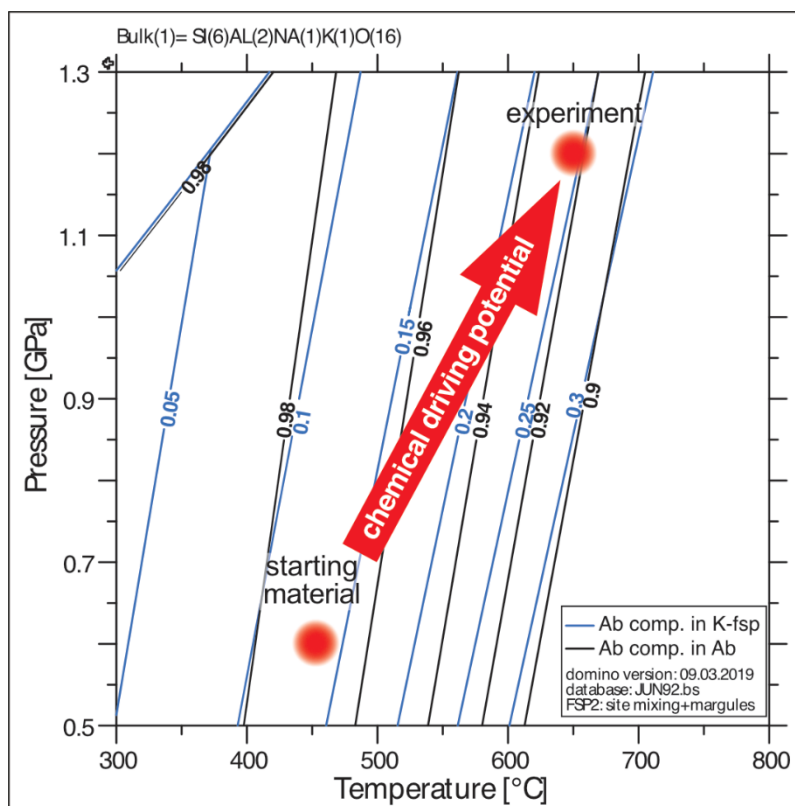
**Figure 10: Pressure-Temperature phase diagram calculated for a two-feldspar system K-feldspar (K-fsp) and albite (ab). The difference in feldspar composition between the starting material and that of the experimental condition induces a chemical driving potential towards the stable composition at experimental P,T-conditions, where ab incorporates more K-fsp component and K-fsp more ab.**

400

### 4.1.4 Role of porosity

The observed DPC differs from classical diffusion creep (Nabarro-Herring creep or Coble creep) by possible advective transport of fluid and/or diffusional transport in a local bulk fluid or distributed fluid film. Porosity and permeability affect the deformation processes by enhancing fluid pathways. Therefore, fluid pathways and porosity are important parameters to evaluate and compare between experiments. In our experiments, two types of porosity are observed: (1) brittle dilatation forming during loading or at peak stress, and (2) shearing induced creep cavities forming during DPC.

The first type of porosity is observed in Type I experiments, where the initial fracture formation results in the creation of a significant quantity of localized porosity (Fig. 4). This porosity and permeability permit the migration of fluid to the comminuted grains. In conjunction with the fine grain size, this porosity is instrumental in achieving near steady-state conditions in an efficient manner. With increasing viscous deformation, the grain size decreases further, the fractured aggregates compact, and the porosity decreases. With increasing strain, local stress differences may allow new phases to grow in between stretched and separated grains, like the K-fsp1 in Fig. 6d,h with bt2 growing around it. Especially at highest strain, the original fracture-induced porosity is almost entirely lost through compaction and growth of minerals (Figs. 4-6).

In Type II experiments, conjugate shear zones form, as seen in low strain experiments, where locally minor porosity is created. The deformation does not localize in these zones, but this local porosity might serve as fluid pathways. At high strains, these openings are closed (Fig. 4). The main shear plane follows the primary mylonitic foliation and is partially influenced by sample geometry (e.g. bottom piston) and does not follow these initial openings. Hence, the role of the initial porosity is negligible, especially compared to pre-fractured samples.

The second type of porosity forms during the deformation at triple grain boundaries and grain boundaries (Fig. 8) and is a result of grain boundary sliding (GBS). New grains nucleate in these cavities (Fig. 8d). Indications for these creep-cavities (Fusseis et al., 2009) are observed in both types of experiments (Figs. 5c, 6i, 8). In both experiment types, only very little of this type of porosity remains, because nucleation and growth rapidly and efficiently fill any cavity formed during DPC and GBS. As these pores appear isolated, diffusive mass transport must occur along grain and interphase boundaries. This process is likely to be accommodated by GBS in a manner similar to the granular fluid pump during creep cavitation (Fusseis et al., 2009).

## 4.2 Applications to nature: The role of grain size and preexisting fracture for the onset of DPC in polymineralic shear zones

430 **4.2.1 (Steady state) grain sizes and flow stresses**

An important point for reconstructing the shear zone evolution in natural rocks is whether the grain size is stable at certain strain rates, pressures, and temperatures. One key factor for models will be the surface energy of a system that is increased by grain size reduction or reduced by grain growth. The grain growth and grain size reduction rates may balance each other at steady state. From such an assumption, combined with internal energy contributions, (i.e., dislocation density), grain size

435 piezometers (e.g. Derby, 1991; Twiss, 1977), and P,T & strain rate sensitive paleowattmeters (Austin and Evans, 2007, 2009) are developed. Our experiments show that an additional parameter for the total energy budget of the shear zone in both settings is the chemical driving potential of constituent phases (e.g., feldspars and biotites). The chemical driving potential of metastable phases enhances the dissolution rate in samples during DPC and thus may contribute to enhancing the strain rate. In any case, the metastability needs to be considered in the energy balance for potential steady state conditions. At the same

440 time, pinning inhibits the grain growth leading to a mechanically weak stable microstructure. Many case studies estimate stresses and strain rates from grain sizes calibrated for dislocation creep regimes in monomineralic systems that lack chemical driving and pinning components. Consequently, neither piezometers nor paleowattmeters are thought to be applicable to DPC in polymineralic rocks.

In some recent studies, paleowattmeter have been applied to diffusion creep systems (Ruh et al., 2024; Tokle and Hirth, 2021)

445 but chemical driving potentials, nucleation rates, or other diffusion parameters and polymineralic chemistry are not included. It is implied that feldspar grain size reduction leads to a very fine grain size, resulting in deformation in the diffusion creep regime, while quartz remains deforming by dislocation creep. Tokle and Hirth (2021) have calibrated the paleowattmeter to match quartz experiments. To evaluate the applicability of paleowattmeters to the granitoid system at our experimental conditions, we first need to assess the representative stable grain size at corresponding stresses and strain rates in our

450 experiments.

Provided the strain is progressively localizing in narrower zones during the whole deformation history, then the strain rate is increasing in the narrowing deforming zone. In experiment Type I we assume that at peak stress the coarse, earlier formed, grains were predominantly accommodating strain in the originally wider zone. During subsequent stages, the near-steady-state-stress is accommodated within the more localized zones consisting of smaller grains. We hence obtain two systems in

455 the same experiment, with two stresses (peak and flow stress), and two different grain sizes and strain rates. This technique gives parameters to evaluate a potential strain rate - grain size sensitivity in these rocks, which we also used to estimate approximate grain size exponents for a constitutive equation in companion paper 2.

Although strain in the not-pre-cracked Type II experiments is more distributed, the observed mechanical weakening and localized grain size reduction at grain/phase boundaries indicates that these experiments have not reached steady state

460 microstructures yet. The strain rate is not homogeneous, and two end member strain rates are active at the same time: A slower

strain rate for the large grains and a fast strain rate for the narrow fine-grained zones in between. If mostly the fine grains are accommodating the strain (interconnected weak layers; e.g., Handy, 1994), the bulk strain rate will underestimate the actual strain rate of these fine-grained zones.

The DPC of type II shear zones is distributed over larger regions of the samples and there still is a large volume of primary
465   grains preserved. From observations of the pores, we infer that "S"-grains represent the grain size of newly nucleated grains, followed by grain growth to a grain size of "L" grains. This grain size reduction achieved through nucleation during DPC and GBS is very efficient and leads to grain sizes comparable to "medium strain" stages in Type I experiments (Fig. 9). The continuous deformation of a not pre-fractured rock would either lead to a homogeneous sample with L grain sizes, or to localizing in throughgoing narrower shear zones, where the grain size will decrease after sufficient strain and further grain size
470   reduction by nucleation and phase mixing.

Tokle and Hirth (2021) have shown that the calibrated piezometer would overestimate the grain size of other grain growth laws if they are based on microstructures where pinning with secondary phases occurs (i.e. Wightman et al., 2006). Indeed, inserting approximate values from our experiments into the Tokle and Hirth (2021) calibrated paleowattmeter results in grain sizes of ~260nm for 500MPa differential stress and $10^{-3}s^{-1}$ strain rate (as in Type I experiments) or ~2μm for 200MPa
475   differential stress and $10^{-6}s^{-1}$ (as in Type II experiments), which is one order of magnitude larger than the observed grain sizes developed through DPC in our experiments. Even if a faster strain rate is assumed in the localized zones, the piezometer overestimates the grain size or would underestimate the actual stresses in natural polymineralic mylonites, where DPC is the dominant deformation mechanism.

Despite the lack of a grain growth inhibiting term and a term for chemical driving potential or nucleation rates, the original
480   paleowattmeter (Austin and Evans, 2007), predicts grain sizes of ~20 nm in Type I experiments and ~150 nm in Type II as flow stresses and strain rates of monomineralic quartz aggregates. Surprisingly, these values are in agreement with the range of grain sizes observed during the experiments: 150-10 nm in Type I, 200-50 nm in Type II. Therefore, our study opens the question whether in some cases the paleowattmeter could predict the stresses from grain sizes in polymineralic shear zones that formed through DPC. In this case, pinning in polymineralic rocks must be counterbalanced by very efficient/fast nucleation
485   and growth rates leading to the self-sustaining and balanced system with a stable grain size. It should be mentioned though that creep data of quartz for these grain sizes and strain rates are not available from experiments, so that the extrapolation goes way out of the existing data range. More experiments are needed to confirm this observation and to improve corresponding flow laws used to build the paleowattmeters.

For a quartzo-calcitic polymineralic system (calcareous shales), Gratier et al. (2023) recently published a flow law including
490   the diffusive and grain boundary sliding parameters. It is to be noted that for granitoid rocks still a flow law is required, which considers reaction kinetics, chemical driving forces, diffusion pathway lengths and other rate limiting steps to quantitatively describe the stress/grain size relationships.

### 4.2.2 Strain localization mechanisms

Under natural greenschist facies metamorphic conditions, ample evidence exists that in the middle to upper granitoid crust
495   deformation is strongly localized in fine-grained polymineralic ultramylonites being surrounded by coarse-grained low to
moderate strain domains (Choukroune and Gapais, 1983; Fitz Gerald and Stünitz, 1993; Marquer et al., 1985; Stünitz and Fitz
Gerald, 1993; Wehrens et al., 2016). Two general types of strain localization have been observed: (i) classical gradual strain
localization across strain gradients and (ii) quasi abrupt changes along sharp contacts from non/weak- to highly localized
deformation. (ii) Has been interpreted as strain-localization via brittle precursor microfractures (e.g., Fitz Gerald and Stünitz,
500   1993), followed by a viscous deformation that may or may not follow a mesoscopic brittle fracture (e.g. Fitz Gerald and Stünitz,
1993; Stünitz and Fitz Gerald, 1993; Mancktelow and Pennacchioni, 2005; Pennacchioni and Mancktelow, 2007; Wehrens et
al., 2016). The mesoscopic fracture may be absent, indicating that the important features for the initiation of viscous
deformation are the microfractures (which may accompany the mesoscopic fracture as a damage zone). In contrast, (i) evolved
as a progressive ductile strain localization (e.g. Choukroune and Gapais, 1983; Marquer et al., 1985; Wehrens et al., 2016). In
505   the case of the Aar Massif (Basement outcrops in central Switzerland), Wehrens et al. (2016) observed a tendency for (i) and
(ii) localization in plutonites with granitic and granodioritic compositions, respectively. A ~5-10 vol% increased content of
interconnected sheet silicates in the latter case, is thought to promote a viscous strain localization behavior. Although having
been performed at amphibolite metamorphic conditions, our new Type I and II experiments can now contribute substantially
to an improved knowledge on the difference between these two end-member strain localization behaviors observed in nature
510   under greenschist to amphibolite facies metamorphic conditions. Our experiments demonstrate that a definite relationship
between bulk and localized strain rates, grain size evolution and the role of grain size, porosity, and local phase composition
exists for DPC in polymineralic rocks: Owing to its grain size sensitivity, diffusion /dissolution precipitation creep (DPC) is
known to dominate as deformation mechanism in fine-grained rocks at elevated temperature conditions resulting in a weak
rheology of the deforming rock. In the case of granitoid rocks with grain sizes in the range of millimeters to centimeters, grain
515   sizes are too large to allow for an efficient deformation by DPC. Hence, to activate DPC in an initially coarse-grained natural
rock, some precursor mechanism reducing the grain size is always required (leading to phase mixing and subsequent activation
of DPC): e.g. (1) a brittle grain size comminution (Bürgmann and Dresen, 2008; Fitz Gerald and Stünitz, 1993; Menegon et
al., 2013) or (2) the initiation of dynamic recrystallization (dislocation creep) until a fine grain size is reached (Bercovici and
Skemer, 2017; Ricard and Bercovici, 2009; Rutter and Brodie, 1988; Schmid, 1982) or (3) reaction with nucleation of small
520   sized new phases (Ceccato et al., 2018; Fitz Gerald and Stünitz, 1993; Mansard et al., 2020a, b; Marti et al., 2017, 2018;
Menegon et al., 2008; Stünitz and Tullis, 2001).

Similar to the observed end member localization behaviors in nature, our experiments show two types of grain size reducing
mechanisms in granitoid polymineralic rocks: (1) Brittle fracturing, which reduces the grain size significantly (Fig. 4d); (2)
Reaction of different phases due to chemical driving potentials when being exposed to a differential stress (Figs. 5, 6, 7, 11).
525   Accompanying grain boundary sliding, DPC is directly activated at phase boundaries in the latter case. This relationship of

processes demonstrates that initial brittle deformation at the microscale, combined with other processes, is one end-member precursor to localize strain. Similar microstructures have been observed in many natural settings by, e.g. Bürgmann and Dresen, 2008 (and references therein), Fitz Gerald and Stünitz (1993). Mesoscopic fractures may or may not be associated with such brittle microscale grain comminution (Goncalves et al., 2016; Mancktelow and Pennacchioni, 2005; Pennacchioni and
530 Mancktelow, 2007), but also reaction weakening can be very effective instead, as also observed on natural faults by, e.g., Ceccato et al., 2018; Menegon et al., 2008Hence, both, strain localization and more distributed strain, may form in granitoids in nature. In both cases the stresses are decreasing due to an increased activity of DPC. In terms of the rheological behavior of the two end member localization mechanisms in nature, our results indicate that fracture-induced strain localization reaches weaker DPC rheologies after lower acquired strains compared to the purely viscous strain localization. Therefore, the lower
535 the deformation temperature in granitoid rocks, the more efficient fracture-induced initiation of DPC-assisted strain localization is. At high finite strains, the mechanical strength of both localization types might be rather similar once polymineralic DPC steady-state microstructures evolved, as can also be inferred from the grain size evolution (Fig. 9f).

An important parameter which is still poorly understood in natural shear zones is the level of inhomogeneity needed to efficiently support localization of strain (Ceccato et al., 2022). At our experimental conditions brittle grain size reduction
540 initiates DPC in a very narrow zone and is always leading to strain localization. The less localized deformation in Type II experiments, i.e., no localized deformation of more fine-grained or more mixed mylonitic bands compared to initial fsp-qtz rich bands indicates that the rheological contrast between the mylonitic bands was not sufficient for strain localization. Thus, not every inhomogeneity in a granitoid rock may serve as an agent for strain localization, so that the rheological evolution of the granitoid system may vary (as in section 4.1.2). The key differences between the deforming systems are the initial grain
545 sizes and porosity. More experiments are necessary to further estimate the influence of phase mixing, porosity and grain size, by e.g. gradually modifying grain sizes and compositions.

## 5 Summary and Conclusions

Two types of experiments on a natural granitoid ultramylonite were performed at 650°C and 1.2 GPa confining pressure. In Type I experiments, an early induced brittle fracture served as precursor for the initiation of localized deformation through
550 dissolution and precipitation creep (DPC). The final deformation required only low differential stresses of ~500 MPa at fast strain rates of ~$10^{-3}$m s$^{-1}$. In coaxial Type II experiments, deformation initiated through reactions at phase boundaries and led to distributed DPC. The distributed strain resulted in continuous strain weakening to <200 MPa at strain rates of ~$10^{-6}$m s$^{-1}$. Evaluation of the strain evolution in the experiments highlights that grain sizes, porosity, and chemical driving potential are important driving forces for the activation of DPC and localization of strain. During deformation, grain growth is inhibited
555 through phase mixing and pinning, which results in continuous deformation in the DPC field. However, the initial grain size and porosity define whether the deformation localizes directly or if distributed small grain size domains are created and are continuously widened. Chemical gradients caused by mineral metastability in combination with the distribution of the

minerals/phases at given physico-chemical deformation conditions, may play an important role for both, the localization processes as well as the preservation of microstructural steady state. Comparisons with other polymineralic studies indicate

560    that these processes are applicable to a broad range of mineral assemblages.
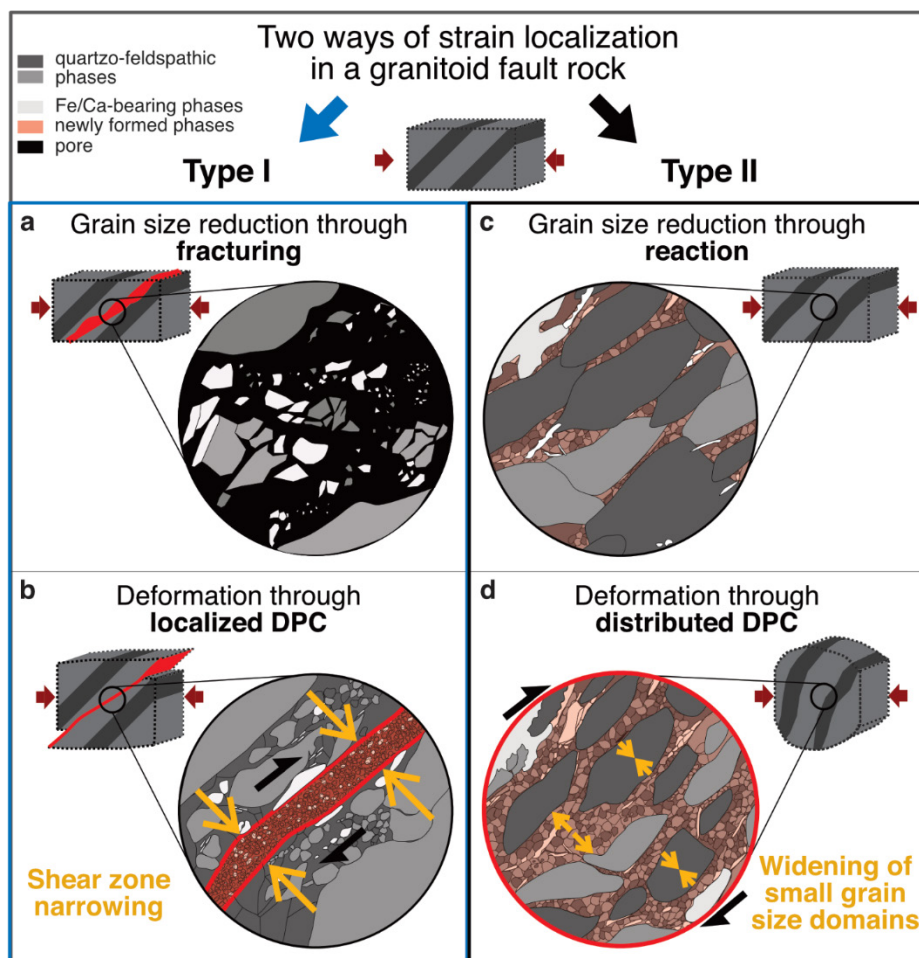
**Figure 11: Summary of the different grain size reduction and strain localization mechanisms. The schematic microstructures are drawn as seen in SEM images. Independent of the initial grain size reducing mechanism, grain boundary sliding accommodated by dissolution precipitation creep (DPC) is accommodating the strain in granitoid fine-grained rocks. Pinning of grain growth leads to a stable microstructure. If a fracture is created (a), that reduces the grain size, then the deformation will localize within the fracture and deform in a very narrow, very fine-grained zone deforming by DPC (bound by red lines in b). If no fracture exists, reactions between minerals will lead to grain size reduction (c) and subsequent activation of DPC. In this case, the deformation is distributed (red circle in d).**

*Code availability/Data availability:* All images and data are included in the article and supplementary material or referenced in the text.

565 *Author contributions:* NN, MH, AB: conceptualization, NN: writing (original draft). MH and AB: funding acquisition, supervision, and project administration. NN, HS, MH, AB: methodology and investigation. NN and WZ: joined training at the experimental machines by HS and experimental data acquisition (5 exp. together, then NN alone). MO: operator (S)TEM at EM Centre, where OP: facility manager. MH, AB, HS, OP and WZ: writing (review and editing), NN: writing (final draft).

570 *Competing interests:* The contact author has declared that none of the authors has any competing interests.

*Acknowledgements:* This project has received funding from the European Union's Horizon 2020 research and innovation programme the EXCITE Network (www.excite-network.eu) under grant agreement No 101005611 for Transnational Access conducted at EM Centre.

*Financial support:* This work has been funded by the Swiss National Science Foundation (SNSF) grant number 192124 to
575 MH.

## References

EXCITE Network: https://excite-network.eu/, last access: 13 September 2024.

Arzt, E., Ashby, M. F., and Verrall, R. A.: Interface controlled diffusional creep, Acta Metallurgica, 31, 1977–1989, https://doi.org/10.1016/0001-6160(83)90015-9, 1983.

580 Austin, N. J. and Evans, B.: Paleowattmeters: A scaling relation for dynamically recrystallized grain size, Geol, 35, 343, https://doi.org/10.1130/G23244A.1, 2007.

Austin, N. J. and Evans, B.: The kinetics of microstructural evolution during deformation of calcite, J. Geophys. Res., 114, B09402, https://doi.org/10.1029/2008JB006138, 2009.

Behrmann, J. H. and Mainprice, D.: Deformation mechanisms in a high-temperature quartz-feldspar mylonite: evidence for
585 superplastic flow in the lower continental crust, Tectonophysics, 140, 297–305, https://doi.org/10.1016/0040-1951(87)90236-8, 1987.

Bercovici, D. and Karato, S. -i.: Theoretical Analysis of Shear Localization in the Lithosphere, Reviews in Mineralogy and Geochemistry, 51, 387–420, https://doi.org/10.2138/gsrmg.51.1.387, 2002.

Bercovici, D. and Ricard, Y.: Plate tectonics, damage and inheritance, Nature, 508, 513–516,
590 https://doi.org/10.1038/nature13072, 2014.

Bercovici, D. and Skemer, P.: Grain damage, phase mixing and plate-boundary formation, Journal of Geodynamics, 108, 40–55, https://doi.org/10.1016/j.jog.2017.05.002, 2017.

Brodhag, S. H., Herwegh, M., and Berger, A.: Grain coarsening in polymineralic contact metamorphic carbonate rocks: The role of different physical interactions during coarsening, Journal of Structural Geology, 33, 698–712, https://doi.org/10.1016/j.jsg.2010.12.003, 2011.

Bürgmann, R. and Dresen, G.: Rheology of the Lower Crust and Upper Mantle: Evidence from Rock Mechanics, Geodesy, and Field Observations, Annu. Rev. Earth Planet. Sci., 36, 531–567, https://doi.org/10.1146/annurev.earth.36.031207.124326, 2008.

Ceccato, A., Menegon, L., Pennacchioni, G., and Morales, L. F. G.: Myrmekite and strain weakening in granitoid mylonites, Solid Earth, 9, 1399–1419, https://doi.org/10.5194/se-9-1399-2018, 2018.

Ceccato, A., Goncalves, P., and Menegon, L.: On the petrology and microstructures of small-scale ductile shear zones in granitoid rocks: An overview, Journal of Structural Geology, 161, 104667, https://doi.org/10.1016/j.jsg.2022.104667, 2022.

Challandes, N., Marquer, D., and Villa, I. M.: P-T-t modelling, fluid circulation, and 39Ar-40Ar and Rb-Sr mica ages in the Aar Massif shear zones (Swiss Alps), Swiss J. Geosci., 101, 269–288, https://doi.org/10.1007/s00015-008-1260-6, 2008.

Choukroune, P. and Gapais, D.: Strain pattern in the Aar Granite (Central Alps): Orthogneiss developed by bulk inhomogeneous flattening, Journal of Structural Geology, 5, 411–418, https://doi.org/10.1016/0191-8141(83)90027-5, 1983.

Derby, B.: The dependence of grain size on stress during dynamic recrystallisation, Acta Metallurgica et Materialia, 39, 955–962, https://doi.org/10.1016/0956-7151(91)90295-C, 1991.

Ebert, A., Herwegh, M., Evans, B., Pfiffner, A., Austin, N., and Vennemann, T.: Microfabrics in carbonate mylonites along a large-scale shear zone (Helvetic Alps), Tectonophysics, 444, 1–26, https://doi.org/10.1016/j.tecto.2007.07.004, 2007.

Ebert, A., Herwegh, M., Berger, A., and Pfiffner, A.: Grain coarsening maps for polymineralic carbonate mylonites: A calibration based on data from different Helvetic nappes (Switzerland), Tectonophysics, 457, 128–142, https://doi.org/10.1016/j.tecto.2008.05.007, 2008.

Elliott, D.: Diffusion Flow Laws in Metamorphic Rocks, Geol Soc America Bull, 84, 2645, https://doi.org/10.1130/0016-7606(1973)84<2645:DFLIMR>2.0.CO;2, 1973.

Etheridge, M. A., Wall, V. J., Cox, S. F., and Vernon, R. H.: High fluid pressures during regional metamorphism and deformation: Implications for mass transport and deformation mechanisms, J. Geophys. Res., 89, 4344–4358, https://doi.org/10.1029/JB089iB06p04344, 1984.

Fitz Gerald, J. D. and Stünitz, H.: Deformation of granitoids at low metamorphic grade. I: Reactions and grain size reduction, Tectonophysics, 221, 269–297, https://doi.org/10.1016/0040-1951(93)90163-E, 1993.

Fuhrman, M. L. and Lindsley, D. H.: Ternary-feldspar modeling and thermometry, American Mineralogist, 73, 201–215, 1988.

Fukuda, J., Holyoke III, C. W., and Kronenberg, A. K.: Deformation of Fine-Grained Quartz Aggregates by Mixed Diffusion and Dislocation Creep, Journal of Geophysical Research: Solid Earth, 123, 4676–4696, https://doi.org/10.1029/2017JB015133, 2018.

Fusseis, F., Regenauer-Lieb, K., Liu, J., Hough, R. M., and De Carlo, F.: Creep cavitation can establish a dynamic granular fluid pump in ductile shear zones, Nature, 459, 974–977, https://doi.org/10.1038/nature08051, 2009.

Ghosh, S., Stünitz, H., Raimbourg, H., and Précigout, J.: Quartz rheology constrained from constant-load experiments: Consequences for the strength of the continental crust, Earth and Planetary Science Letters, 597, 117814, https://doi.org/10.1016/j.epsl.2022.117814, 2022.

630 Ghosh, S., Stünitz, H., Raimbourg, H., Précigout, J., Di Carlo, I., Heilbronner, R., and Piani, L.: Importance of grain boundary processes for plasticity in the quartz-dominated crust: Implications for flow laws, Earth and Planetary Science Letters, 640, 118767, https://doi.org/10.1016/j.epsl.2024.118767, 2024.

Gilgannon, J., Fusseis, F., Menegon, L., Regenauer-Lieb, K., and Buckman, J.: Hierarchical creep cavity formation in an ultramylonite and implications for phase mixing, Solid Earth, 8, 1193–1209, https://doi.org/10.5194/se-8-1193-2017, 2017.

635 Gilgannon, J., Waldvogel, M., Poulet, T., Fusseis, F., Berger, A., Barnhoorn, A., and Herwegh, M.: Experimental evidence that viscous shear zones generate periodic pore sheets, Solid Earth, 12, 405–420, https://doi.org/10.5194/se-12-405-2021, 2021.

Goncalves, P., Oliot, E., Marquer, D., and Connolly, J. A. D.: Role of chemical processes on shear zone formation: an example from the Grimsel metagranodiorite (Aar massif, Central Alps): SHEAR ZONE FORMATION, Journal of Metamorphic 640 Geology, 30, 703–722, https://doi.org/10.1111/j.1525-1314.2012.00991.x, 2012.

Goncalves, P., Poilvet, J.-C., Oliot, E., Trap, P., and Marquer, D.: How does shear zone nucleate? An example from the Suretta nappe (Swiss Eastern Alps), Journal of Structural Geology, 86, 166–180, https://doi.org/10.1016/j.jsg.2016.02.015, 2016.

Gratier, J., Guiguet, R., Renard, F., Jenatton, L., and Bernard, D.: A pressure solution creep law for quartz from indentation experiments, J. Geophys. Res., 114, 2008JB005652, https://doi.org/10.1029/2008JB005652, 2009.

645 Gratier, J., Menegon, L., and Renard, F.: Pressure Solution Grain Boundary Sliding as a Large Strain Mechanism of Superplastic Flow in the Upper Crust, JGR Solid Earth, 128, e2022JB026019, https://doi.org/10.1029/2022JB026019, 2023.

Gratier, J.-P., Dysthe, D. K., and Renard, F.: The Role of Pressure Solution Creep in the Ductility of the Earth's Upper Crust, in: Advances in Geophysics, vol. 54, Elsevier, 47–179, https://doi.org/10.1016/B978-0-12-380940-7.00002-0, 2013.

Gueydan, F., Leroy, Y. M., Jolivet, L., and Agard, P.: Analysis of continental midcrustal strain localization induced by 650 microfracturing and reaction-softening: CONTINENTAL MIDCRUSTAL STRAIN LOCALIZATION, J. Geophys. Res., 108, https://doi.org/10.1029/2001JB000611, 2003.

Handy, M. R.: Flow laws for rocks containing two non-linear viscous phases: A phenomenological approach, Journal of Structural Geology, 16, 287–301, https://doi.org/10.1016/0191-8141(94)90035-3, 1994.

Herwegh, M. and Jenni, A.: Granular flow in polymineralic rocks bearing sheet silicates: new evidence from natural examples, 655 Tectonophysics, 332, 309–320, https://doi.org/10.1016/S0040-1951(00)00288-2, 2001.

Herwegh, M., de Bresser, J. H. P., and ter Heege, J. H.: Combining natural microstructures with composite flow laws: an improved approach for the extrapolation of lab data to nature, Journal of Structural Geology, 27, 503–521, https://doi.org/10.1016/j.jsg.2004.10.010, 2005.

Herwegh, M., Linckens, J., Ebert, A., Berger, A., and Brodhag, S. H.: The role of second phases for controlling microstructural 660 evolution in polymineralic rocks: A review, Journal of Structural Geology, 33, 1728–1750, https://doi.org/10.1016/j.jsg.2011.08.011, 2011.

Hippertt, J. F.: Breakdown of feldspar, volume gain and lateral mass transfer during mylonitization of granitoid in a low metamorphic grade shear zone, Journal of Structural Geology, 20, 175–193, https://doi.org/10.1016/S0191-8141(97)00083-7, 1998.

Hirth, G. and Tullis, J.: The brittle-plastic transition in experimentally deformed quartz aggregates, J. Geophys. Res., 99, 11731–11747, https://doi.org/10.1029/93JB02873, 1994.

Hirth, G., Teyssier, C., and Dunlap, J. W.: An evaluation of quartzite flow laws based on comparisons between experimentally and naturally deformed rocks, Int J Earth Sci, 90, 77–87, https://doi.org/10.1007/s005310000152, 2001.

Imon, R., Okudaira, T., and Fujimoto, A.: Dissolution and precipitation processes in deformed amphibolites: an example from the ductile shear zone of the Ryoke metamorphic belt, SW Japan, Journal Metamorphic Geology, 20, 297–308, https://doi.org/10.1046/j.1525-1314.2002.00367.x, 2002.

Imon, R., Okudaira, T., and Kanagawa, K.: Development of shape- and lattice-preferred orientations of amphibole grains during initial cataclastic deformation and subsequent deformation by dissolution–precipitation creep in amphibolites from the Ryoke metamorphic belt, SW Japan, Journal of Structural Geology, 26, 793–805, https://doi.org/10.1016/j.jsg.2003.09.004, 2004.

Kilian, R., Heilbronner, R., and Stünitz, H.: Quartz grain size reduction in a granitoid rock and the transition from dislocation to diffusion creep, Journal of Structural Geology, 33, 1265–1284, https://doi.org/10.1016/j.jsg.2011.05.004, 2011.

Lee, A. L., Stünitz, H., Soret, M., and Battisti, M. A.: Dissolution precipitation creep as a process for the strain localisation in mafic rocks, Journal of Structural Geology, 155, 104505, https://doi.org/10.1016/j.jsg.2021.104505, 2022.

Linckens, J., Herwegh, M., Müntener, O., and Mercolli, I.: Evolution of a polymineralic mantle shear zone and the role of second phases in the localization of deformation, J. Geophys. Res., 116, B06210, https://doi.org/10.1029/2010JB008119, 2011.

Linckens, J., Herwegh, M., and Müntener, O.: Small quantity but large effect — How minor phases control strain localization in upper mantle shear zones, Tectonophysics, 643, 26–43, https://doi.org/10.1016/j.tecto.2014.12.008, 2015.

Mancktelow, N. S. and Pennacchioni, G.: The control of precursor brittle fracture and fluid–rock interaction on the development of single and paired ductile shear zones, Journal of Structural Geology, 27, 645–661, https://doi.org/10.1016/j.jsg.2004.12.001, 2005.

Mansard, N., Raimbourg, H., Augier, R., Précigout, J., and Le Breton, N.: Large-scale strain localization induced by phase nucleation in mid-crustal granitoids of the south Armorican massif, Tectonophysics, 745, 46–65, https://doi.org/10.1016/j.tecto.2018.07.022, 2018.

Mansard, N., Stünitz, H., Raimbourg, H., Précigout, J., Plunder, A., and Nègre, L.: Relationship between microstructures and resistance in mafic assemblages that deform and transform, Solid Earth, 11, 2141–2167, https://doi.org/10.5194/se-11-2141-2020, 2020a.

Mansard, N., Stünitz, H., Raimbourg, H., and Précigout, J.: The role of deformation-reaction interactions to localize strain in polymineralic rocks: Insights from experimentally deformed plagioclase-pyroxene assemblages, Journal of Structural Geology, 134, 104008, https://doi.org/10.1016/j.jsg.2020.104008, 2020b.

Marquer, D., Gapais, D., and Capdevila, R.: Comportement chimique et orthogneissification d'une granodiorite en faciès schistes verts (Massif de l'Aar, Alpes centrales), bulmi, 108, 209–221, https://doi.org/10.3406/bulmi.1985.7869, 1985.

Marti, S., Heilbronner, R., Stuenitz, H., Pluemper, O., and Drury, M.: Solution-mass transfer and grain boundary sliding in mafic shear zones; comparison between experiments and nature., Geophysical Research Abstracts, 19, Abstract EGU2017-3203, 2017.

Marti, S., Stünitz, H., Heilbronner, R., Plümper, O., and Kilian, R.: Syn-kinematic hydration reactions, grain size reduction, and dissolution–precipitation creep in experimentally deformed plagioclase–pyroxene mixtures, Solid Earth, 9, 985–1009, https://doi.org/10.5194/se-9-985-2018, 2018.

Menegon, L., Pennacchioni, G., and Spiess, R.: Dissolution-precipitation creep of K-feldspar in mid-crustal granite mylonites, Journal of Structural Geology, 30, 565–579, https://doi.org/10.1016/j.jsg.2008.02.001, 2008.

Menegon, L., Stünitz, H., Nasipuri, P., Heilbronner, R., and Svahnberg, H.: Transition from fracturing to viscous flow in granulite facies perthitic feldspar (Lofoten, Norway), Journal of Structural Geology, 48, 95–112, https://doi.org/10.1016/j.jsg.2012.12.004, 2013.

Nibourel, L., Berger, A., Egli, D., Heuberger, S., and Herwegh, M.: Structural and thermal evolution of the eastern Aar Massif: insights from structural field work and Raman thermometry, Swiss J Geosci, 114, 9, https://doi.org/10.1186/s00015-020-00381-3, 2021.

Niemeijer, A. R., Spiers, C. J., and Bos, B.: Compaction creep of quartz sand at 400–600°C: experimental evidence for dissolution-controlled pressure solution, Earth and Planetary Science Letters, 195, 261–275, https://doi.org/10.1016/S0012-821X(01)00593-3, 2002.

Okamoto, A. and Hiraga, T.: A Common Diffusional Mechanism for Creep and Grain Growth in Polymineralic Rocks: Experiments, JGR Solid Earth, 127, e2022JB024638, https://doi.org/10.1029/2022JB024638, 2022.

Olgaard, D. L. and Evans, B.: Effect of Second-Phase Particles on Grain Growth in Calcite, Journal of the American Ceramic Society, 69, C-272-C–277, https://doi.org/10.1111/j.1151-2916.1986.tb07374.x, 1986.

Pec, M.: Experimental Investigation on the Rheology of Fault Rocks, Basel University, 210 pp., 2014.

Pec, M. and Al Nasser, S.: Formation of Nanocrystalline and Amorphous Materials Causes Parallel Brittle-Viscous Flow of Crustal Rocks: Experiments on Quartz-Feldspar Aggregates, J Geophys Res Solid Earth, 126, https://doi.org/10.1029/2020JB021262, 2021.

Pec, M., Stünitz, H., Heilbronner, R., and Drury, M.: Semi-brittle flow of granitoid fault rocks in experiments, Journal of Geophysical Research: Solid Earth, 121, 1677–1705, https://doi.org/10.1002/2015JB012513, 2016.

Pennacchioni, G. and Mancktelow, N. S.: Nucleation and initial growth of a shear zone network within compositionally and structurally heterogeneous granitoids under amphibolite facies conditions, Journal of Structural Geology, 29, 1757–1780, https://doi.org/10.1016/j.jsg.2007.06.002, 2007.

Platt, J. P. and Behr, W. M.: Grainsize evolution in ductile shear zones: Implications for strain localization and the strength of the lithosphere, Journal of Structural Geology, 33, 537–550, https://doi.org/10.1016/j.jsg.2011.01.018, 2011.

Raj, R.: Creep in polycrystalline aggregates by matter transport through a liquid phase, J. Geophys. Res., 87, 4731–4739, https://doi.org/10.1029/JB087iB06p04731, 1982.

Ranalli, G.: Deformation maps in grain-size-stress space as a tool to investigate mantle rheology, Physics of the Earth and Planetary Interiors, 29, 42–50, https://doi.org/10.1016/0031-9201(82)90136-4, 1982.

Ree, J.-H.: Grain boundary sliding and development of grain boundary openings in experimentally deformed octachloropropane, Journal of Structural Geology, 16, 403–418, https://doi.org/10.1016/0191-8141(94)90044-2, 1994.

Ricard, Y. and Bercovici, D.: A continuum theory of grain size evolution and damage, J. Geophys. Res., 114, 2007JB005491, https://doi.org/10.1029/2007JB005491, 2009.

Richter, B., Stünitz, H., and Heilbronner, R.: The brittle-to-viscous transition in polycrystalline quartz: An experimental study, Journal of Structural Geology, 114, 1–21, https://doi.org/10.1016/j.jsg.2018.06.005, 2018.

Ruh, J., Behr, W., and Tokle, L.: Effect of Grain-Size and Textural Weakening in Polyphase Crustal and Mantle Lithospheric Shear Zones, tekt, 2, https://doi.org/10.55575/tektonika2024.2.1.68, 2024.

Rutter, E. H.: A Discussion on natural strain and geological structure - The kinetics of rock deformation by pressure solution, Phil. Trans. R. Soc. Lond. A, 283, 203–219, https://doi.org/10.1098/rsta.1976.0079, 1976.

Rutter, E. H. and Brodie, K. H.: The role of tectonic grain size reduction in the rheological stratification of the lithosphere, Geol Rundsch, 77, 295–307, https://doi.org/10.1007/BF01848691, 1988.

Rybacki, E. and Dresen, G.: Deformation mechanism maps for feldspar rocks, Tectonophysics, 382, 173–187, https://doi.org/10.1016/j.tecto.2004.01.006, 2004.

Schmid, S. M.: Microfabric studies as indicators of deformation mechanisms and flow laws operative in mountain building, Mountain Building Processes, 95–110, 1982.

Stünitz, H. and Fitz Gerald, J. D.: Deformation of granitoids at low metamorphic grade. II: Granular flow in albite-rich mylonites, Tectonophysics, 221, 299–324, https://doi.org/10.1016/0040-1951(93)90164-F, 1993.

Stünitz, H. and Tullis, J.: Weakening and strain localization produced by syn-deformational reaction of plagioclase, Int J Earth Sci, 90, 136–148, https://doi.org/10.1007/s005310000148, 2001.

Sun, H. and Pec, M.: Nanometric flow and earthquake instability, Nat Commun, 12, 6779, https://doi.org/10.1038/s41467-021-26996-0, 2021.

Tokle, L. and Hirth, G.: Assessment of Quartz Grain Growth and the Application of the Wattmeter to Predict Quartz Recrystallized Grain Sizes, JGR Solid Earth, 126, e2020JB021475, https://doi.org/10.1029/2020JB021475, 2021.

Tullis, J.: Deformation of Granitic Rocks: Experimental Studies and Natural Examples, Reviews in Mineralogy and Geochemistry, 51, 51–95, https://doi.org/10.2138/gsrmg.51.1.51, 2002.

Tullis, J. and Yund, R. A.: Experimental deformation of dry westerly granite, Journal of Geophysical Research (1896-1977), 82, 5705–5718, https://doi.org/10.1029/JB082i036p05705, 1977.

Tullis, J. and Yund, R. A.: Dynamic recrystallization of feldspar: A mechanism for ductile shear zone formation, Geol, 13, 238, https://doi.org/10.1130/0091-7613(1985)13<238:DROFAM>2.0.CO;2, 1985.

Tullis, J., Dell'Angelo, L., and Yund, R. A.: Ductile shear zones from brittle precursors in feldspathic rocks: The role of dynamic recrystallization, in: Geophysical Monograph Series, vol. 56, edited by: Duba, A. G., Durham, W. B., Handin, J. W., and Wang, H. F., American Geophysical Union, Washington, D. C., 67–81, https://doi.org/10.1029/GM056p0067, 1990.

Twiss, R. J.: Theory and applicability of a recrystallized grain size paleopiezometer, 115, 1977.

Wehrens, P., Berger, A., Peters, M., Spillmann, T., and Herwegh, M.: Deformation at the frictional-viscous transition: Evidence for cycles of fluid-assisted embrittlement and ductile deformation in the granitoid crust, Tectonophysics, 693, 66–
770   84, https://doi.org/10.1016/j.tecto.2016.10.022, 2016.

Wehrens, P., Baumberger, R., Berger, A., and Herwegh, M.: How is strain localized in a meta-granitoid, mid-crustal basement section? Spatial distribution of deformation in the central Aar massif (Switzerland), Journal of Structural Geology, 94, 47–67, https://doi.org/10.1016/j.jsg.2016.11.004, 2017.

Weyl, P. K.: Pressure solution and the force of crystallization: a phenomenological theory, J. Geophys. Res., 64, 2001–2025,
775   https://doi.org/10.1029/JZ064i011p02001, 1959.

Wheeler, J.: Importance of pressure solution and coble creep in the deformation of polymineralic rocks, J. Geophys. Res., 97, 4579, https://doi.org/10.1029/91JB02476, 1992.

White, S. H., Burrows, S. E., Carreras, J., Shaw, N. D., and Humphreys, F. J.: On mylonites in ductile shear zones, Journal of Structural Geology, 2, 175–187, https://doi.org/10.1016/0191-8141(80)90048-6, 1980.

780   Wightman, R. H., Prior, D. J., and Little, T. A.: Quartz veins deformed by diffusion creep-accommodated grain boundary sliding during a transient, high strain-rate event in the Southern Alps, New Zealand, Journal of Structural Geology, 28, 902–
918, https://doi.org/10.1016/j.jsg.2006.02.008, 2006.